Materials & Design 258 (2025) 114519

Contents lists available at ScienceDirect

Materials & Design

journal homepage: www.elsevier.com/locate/matdes

Synergizing weave-architected wettability with hierarchical fibrous assemblies to design hydrophobic woven fabrics

Siddharth Shukla [a], Yue Wen [b], Imre Szenti [c], Akos Kukovecz [c], Thomas C. Sykes [d], Rhodri Jervis [b,e,*], Amit Rawal [a,f,**]

[a] Department of Textile and Fibre Engineering, Indian Institute of Technology Delhi, Hauz Khas, New Delhi, India
[b] Electrochemical Innovation Lab, Department of Chemical Engineering, University College London, Torrington Place, WC1E 7JE London, United Kingdom
[c] Department of Applied and Environmental Chemistry, University of Szeged, Szeged, Hungary
[d] School of Engineering, University of Warwick, Coventry CV4 7AL, United Kingdom
[e] Advanced Propulsion Lab, Marshgate, University College London, London E20 2AE, United Kingdom
[f] The Swedish School of Textiles, University of Borås, Sweden

ARTICLE INFO

Keywords:
Wettability
Hydrophobicity
Woven fabrics
X-ray microcomputed tomography
Apparent contact angle

ABSTRACT

Engineering liquid-repellent textiles through tailored multi-scale surface morphology and controlled surface chemistry opens pathways to a broad spectrum of advanced technological applications. Woven fabrics exemplify intrinsically rough surfaces with hierarchical topography governed by mesoscale weave geometry and the microscale organization of fibers within the yarn structure. Herein, we systematically investigate the wetting behavior of woven fabrics by establishing structure–property relationships between the apparent water contact angle and multi-scale structural hierarchy along with the equilibrium contact angle of the fiber. Guided by the design principles of multi-scale organization, we predict the apparent contact angles of three distinct woven fabrics comprising polyester, a Kevlar/polytetrafluoroethylene (PTFE) hybrid, and carbon using yarn- and structure-level parameters obtained via X-ray microcomputed tomography (micro-CT) analysis. The predicted apparent contact angle values show good agreement with experimental measurements, particularly when evaluating (an)isotropy of droplet behavior from four different directions. Intriguingly, polyester fabric exhibits the fastest wetting transition, enabled by its tightly packed weave and moderate hydrophilicity of the constituent fibers. Parametric analysis demonstrates that tuning yarn- and structure-level parameters, along with the equilibrium (apparent) contact angle of individual fibers (yarn), can induce superhydrophobic behavior in woven fabrics and predict lower roll-off angles. These findings highlight the pivotal role of multi-scale structural design in governing fabric wettability.

1. Introduction

Wetting is a thermodynamic process in which a liquid spreads over a solid surface, driven by a balancing act of interfacial energies at the three-phase contact line (TCL), proliferating solid–liquid-vapor interactions. The equilibrium contact angle (θ_e) formed at the TCL serves as the primary figure of merit for wettability [1]. The wettability threshold, indicated by an equilibrium contact angle of 90°, marks the shift between hydrophilic ($\theta_e < 90°$) and hydrophobic ($\theta_e > 90°$) surface behavior. This transition is primarily governed by the balancing act between the surface tension of the liquid and the surface energy of the solid [2]. Higher contact angles occur when the cohesive forces within a liquid dominate the adhesive forces between the liquid and the solid surface, resulting in reduced wetting affinity [3].

Hydrophobic behavior is dictated by a synergistic interplay between surface chemistry and mesoscopic topological features [4]. Structured hydrophobic surfaces typically exhibit two wetting regimes – the Wenzel state, where liquid completely conforms to the surface roughness [5], and the Cassie-Baxter state, where the droplet contacts only the asperities while trapping air beneath, forming a solid-air composite interface [6]. Surface roughness creates multiple metastable configurations, each separated by a free energy barrier, which collectively inhibit

* Corresponding author at: Electrochemical Innovation Lab, Department of Chemical Engineering, University College London, Torrington Place, WC1E 7JE London, United Kingdom.
** Corresponding author at: Department of Textile and Fibre Engineering, Indian Institute of Technology Delhi, Hauz Khas, New Delhi, India.
E-mail addresses: rhodri.jervis@ucl.ac.uk (R. Jervis), amit.rawal@hb.se, arawal@iitd.ac.in (A. Rawal).

https://doi.org/10.1016/j.matdes.2025.114519
Received 4 June 2025; Received in revised form 4 August 2025; Accepted 4 August 2025
Available online 5 August 2025

the transition to the Wenzel state [7]. Factoring in the chemical and topographical characteristics of surfaces can aid in the rational design of extremely robust, non-wetting surfaces [8].

Surface roughness featuring overhangs or dual-scale topography can markedly amplify hydrophobicity by promoting liquid repellency [9–14]. Woven fabrics serve as a canonical example of inherently rough surfaces characterized by hierarchical topography arising from both the mesoscale weave architecture and the microscale packing of fibers within constituent yarns [14–20]. This inherent hierarchical roughness is especially beneficial in outdoor textiles, where the engineered woven surface topography synergizes with an applied hydrophobic polymer coating to enhance water-repellency [16,21]. Many commercially available hydrophobic polymer coatings rely on fluorinated compounds, which raise significant environmental and health concerns due to their persistence and bioaccumulation potential, prompting stringent global regulations on their manufacture and use [16,22]. Consequently, a library of analytical models has been developed to predict the design parameters of woven fabrics, potentially eliminating the need for perfluorinated substances (PFS) to achieve the desired hydrophobic performance [17,23–25]. However, most existing models fail to include the full hierarchical topography of woven fabrics, including factors such as weave type, as well as other key fiber, yarn, and structural parameters [16,17,20,23].

The present work systematically investigates the wetting behavior of woven fabrics by correlating the apparent water contact angle with the multi-scale structural hierarchy – namely, the macro-scale fabric architecture, meso-scale yarn arrangement, weave geometry, micro-scale fiber/filament topography and the equilibrium contact angle of the filament. Guided by the design principles of multi-scale structural hierarchy, we predicted the apparent contact angle of three distinct woven fabrics comprising polyester, a hybrid of Kevlar/Polytetrafluoroethylene (PTFE), and carbon. Intriguingly, these materials are employed in high-performance applications where hydrophobicity is a critical prerequisite for ensuring functionality, durability, and resistance to environmental exposure. For instance, polyester fabrics are extensively used in tissue engineering and various medical textile applications, where moderately hydrophobic surfaces have been shown to promote higher cell viability [26], while in antimicrobial textiles, comparable surface properties demonstrate microbial growth inhibition [27]. Similarly, conductive carbon fiber-based woven fabrics serve as hydrophobic gas diffusion layers (GDLs) in polymer electrolyte membrane (PEM) fuel cells, where their controlled wettability prevents pore flooding while maintaining uninterrupted gas transport to the catalyst layer [28]. Further, water-repellent woven fabrics are also critical in protective clothing, offering barriers against chemical splashes, hazardous particulates, and microbial penetration-thereby enhancing safety in industrial and healthcare environments [29]. In outdoor textiles such as tents, jackets, and gear designed for extreme conditions, hydrophobic surfaces improve weather resistance and wearer comfort by minimizing water absorption while maintaining breathability [30]. In filtration systems, surface wettability influences fluid selectivity and flow resistance, where superhydrophobic or partially wetting surfaces can enhance particle capture or enable phase-specific separation [31].

To address the diverse performance needs of these applications, we demonstrate the versatility of our analytical model across a range of material systems. In addition to homogeneous fabrics, we apply the model to predict the apparent contact angle of a hybrid fabric combining hydrophilic Kevlar with hydrophobic PTFE yarns [20], showcasing its wide-ranging applicability to a complex material system. Moreover, key fiber, yarn, and fabric parameters were extracted using X-ray micro-computed tomography (micro-CT) analysis, which were then used as critical inputs for validating the predictive model of the apparent water contact angle of the woven fabrics.

2. Theoretical framework

Woven fabrics are hierarchical structures typically consisting of two sets of orthogonal yarns (warp and weft) interlaced in specific patterns commonly called ‘weave’. The surface topology of woven fabrics depends on yarn structure and weave pattern, which in turn affect wetting behavior. Although yarn may be considered as the building block of a woven fabric, it can be further decomposed into its constituent fibers or filaments, introducing an additional component of hierarchy. Therefore, the wetting behavior of the woven fabric is ultimately influenced by the wetting properties of the individual fibers or filaments. The present work aims to examine the wetting state of woven fabrics by establishing a correlation between the apparent water contact angle at three hierarchical levels: the macro-scale (fabric) structure, the meso-scale (yarn), and the micro-scale (fibers/filaments) and the equilibrium contact angle of the fibers. To facilitate the analysis, the following assumptions have been adopted in the model.

- The yarn cross-section is assumed to follow a lenticular geometry based on the X-ray micro-CT analysis of three typical woven fabrics (see Fig. 1). Note that the lenticular yarn cross-sectional shape is geometrically described by two identical circular arcs facing each other [32,33].
- The constituent filaments present within the yarn are assumed to be arranged in a hexagonal configuration. However, in the case of PTFE yarns, which deviate significantly from this idealized packing arrangement, the yarn is instead approximated as a solid filament due to its high packing fraction and smooth mesoscale surface morphology. This simplification aligns with the modeling approach adopted by Lu et al [34].
- The cross-over yarn at the intersections follows a concatenated curved path based on three-dimensional (3D) structures of the fabrics obtained by X-ray micro-CT analysis.
- The droplet is assumed to be static or nearly static during the contact angle measurement, and evaporation effects are minimal.
- Water droplets typically rest on the top of the fabric surface, where the contact region between the droplet and filaments is smaller than the fiber or filament length due to surface roughness. This behavior suggests that the yarns can be modeled as parallel bundles of filaments – a valid assumption for continuous-filament woven fabrics.

Herein, we initially developed a stepwise theoretical approach to predict the apparent contact angle of woven fabric by modeling the yarn-level contact angle based on the relationship between micro- and meso-scale wetting behavior.

2.1. Apparent contact angle of yarns

In this analysis, filaments are considered to have identical dimensions and are arranged in a regular arrangement in a yarn. Specifically, the two parallel filaments viewed normal to their axes in a yarn tow[1] are geometrically represented as cylinders of defined radius (r), separated by a distance of $2d$, as illustrated in Fig. 2. Here, the liquid meniscus is formed such that the three-phase contact line (TCL) on each cylinder is identified by an inclination angle (α_f), i.e., the angle formed between the vertical axis of the cylindrical cross-section and a radius at the contact point [35].

Similarly, the contact angle has been formed through the liquid phase, which is formed between the tangents at the filament and the meniscus at the TCL, as shown in Fig. 2. Invariably, it is presumed that the contact angle of the liquid depends primarily on molecular

[1] A long bundle of continuous, untwisted filaments used either as an intermediate material for producing staple fibers or as an end product in specific textile applications.

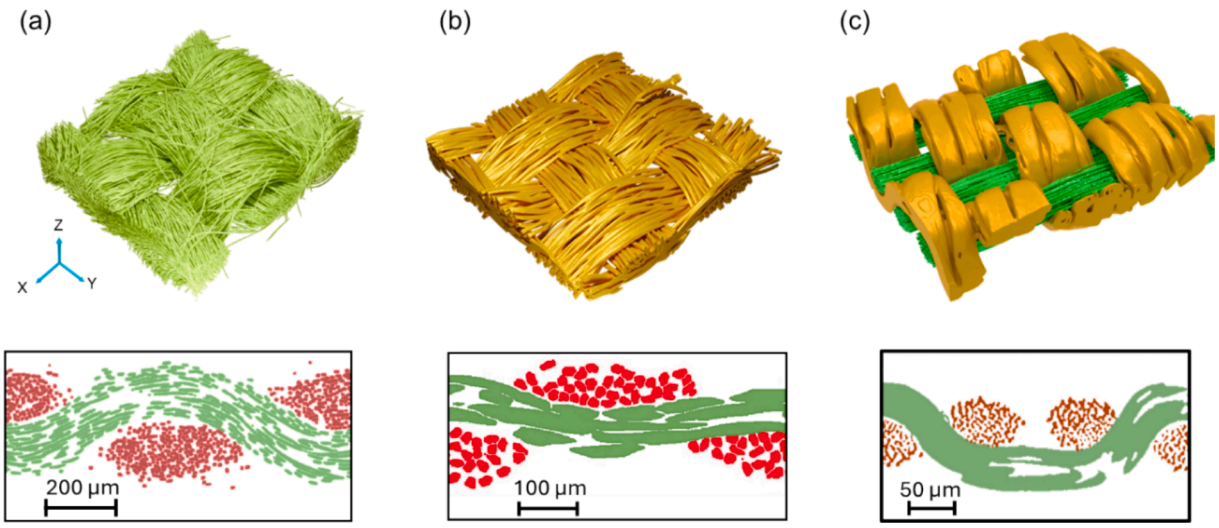

Fig. 1. 3D rendered images of fabric samples (a) F1 (carbon), (b) F2 (polyester) and (c) F3 (Kevlar/PTFE Hybrid), generated from X-ray micro- CT analysis, along with their corresponding cross-sectional views. In Fig. (c), Kevlar fibers display a lenticular cross-section.

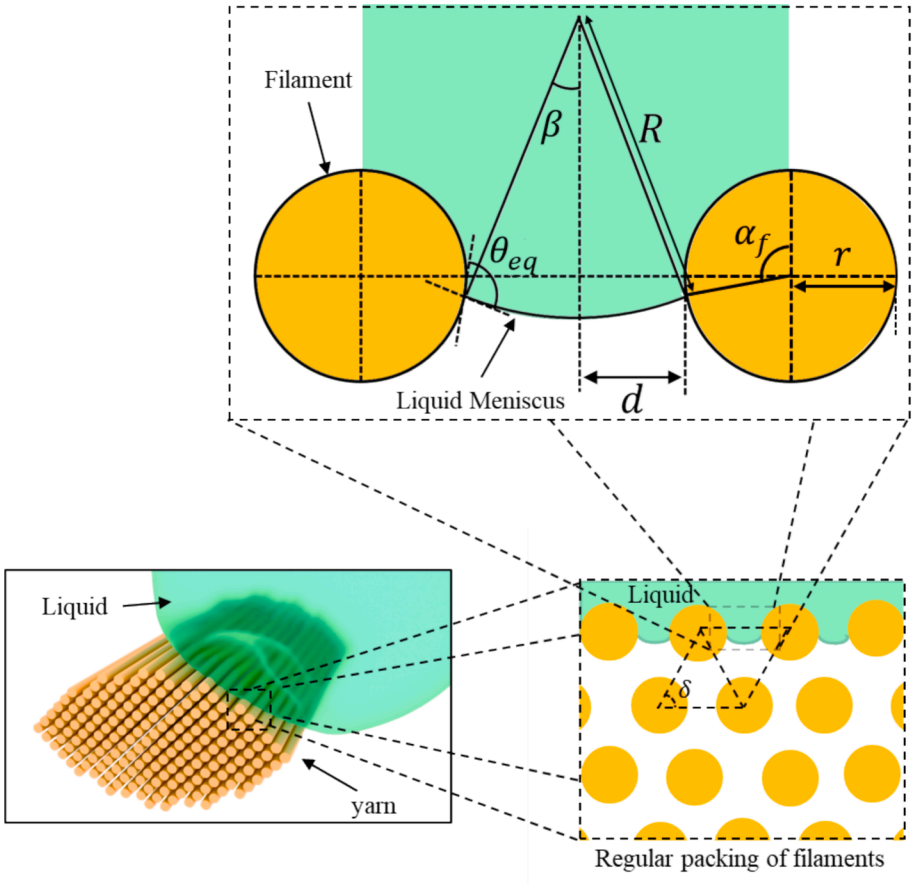

Fig. 2. Schematic depicting the lenticular cross-sectional view of the yarn in contact with the liquid meniscus. Here, the magnified images show the regular packing of filaments in the yarn cross-section and the two neighboring filaments in contact with the liquid meniscus.

interactions present in the close vicinity of TCL rather than the geometry of the system. As the liquid droplet enters the hourglass-shaped capillary between the two filaments, the curvature of the meniscus between the filaments tends to change from minimum to maximum magnitude before it touches the base. While the minimum curvature of the meniscus is obtained as the initial wetting response of the surface upon preliminary contact with the water droplet, it eventually reaches its highest magnitude when maximum wetting resistance is achieved upon droplet stabilization [35]. Consequently, the position of the meniscus contact line on each filament ($\pi - \alpha_f$) can be related to its equilibrium contact angle and other geometrical parameters, as shown below [35],

$$\alpha_f = \cos^{-1}\left[\frac{\sin\theta_{eq}\cos\theta_{eq} \mp \sin\theta_{eq}\sqrt{(S+1)^2 - \sin^2\theta_{eq}}}{S+1}\right] \quad (1)$$

where $S(=d/r)$ is the spacing ratio, θ_{eq} is the equilibrium contact angle of the filaments in yarn, r is the radius of the filament, and d is the half of the distance between the two consecutive filaments [35].

It should be noted that in the original work [35], the positive (+) sign corresponds to the maximum wet-through resistance while considering '$\pi - \alpha_f^{max}$' in Equation (1). Since we are computing 'α_f^{max}', we have used the negative (−) sign in our formulation.

Assuming that the filaments within a yarn tow are laid parallel and arranged in a regular, repeating and rhombic pattern (as illustrated in Fig. 2), the spacing ratio, S, can be expressed as,

$$S = \sqrt{\frac{\pi}{4V_f\sin\delta}} - 1 \quad (2)$$

where V_f denotes the yarn packing fraction (defined as the ratio of the total area occupied by the filaments to the overall cross-sectional area of the yarn), and δ is the acute angle between the two neighboring filaments (see Fig. 2).

For simplicity, $\delta = 60°$, corresponding to hexagonal packing of filaments in a yarn, has been considered, and a detailed derivation of Equation (2) has been provided in the supplementary information. It must be noted that V_f is further influenced by the twisted structure of the yarn. While it is theoretically possible to derive a highly rigorous relationship through detailed geometric and mechanical analysis, the work of Pan [36] suggests that such an expression would likely be excessively complex and of limited practical utility. Consequently, the effect of twist can be accommodated using an empirical expression as follows [36],

$$V_f = V_{fm} - \left(V_{fm} - V_{f_o}\right)e^{-ET_y} \quad (3)$$

where V_{f_o} is the minimum yarn packing fraction, V_{f_m} is the maximum yarn packing fraction that can be achieved by the twisted yarn, $T_y\left(=\frac{\tan\kappa}{\pi D_y}\right)$ is the twist per unit length, κ is the helical (twist) angle of the fibers, D_y is the diameter of a yarn with a circular cross-section and E is an empirical parameter.

Furthermore, determining the value of the empirical parameter for different yarns necessitates a separate experimental evaluation [36]. However, in the present study, yarns exhibit minimal to negligible twist levels, as summarized in Table S1. As a result, the yarn packing fraction values derived from X-ray microCT analysis have been directly used as input for the current model.

A combinatorial strategy involving yarn roughness, porosity, and surface energy may restrict the passage of the liquid into the filaments [15]. A solid–liquid-air interface composite is thus formed by trapping the air pockets underneath the surface texture, and only a fraction of the solid surface is wet. The seminal work of Cassie-Baxter [6] allows the prediction of the apparent contact angle of a composite interface. Accordingly, the apparent contact angle of the yarn (θ_y^*) has been predicted, as shown below.

$$\cos\theta_y^* = f_1^f\cos\theta_{eq} - f_2^f \quad (4)$$

where f_1^f and f_2^f are the area fractions of the solid (filament) /liquid and liquid/air interfaces, respectively.

Based on the elementary definition of f_1^f and f_2^f, the expressions of these parameters are given below [6,35].

$$f_1^f = \frac{r\alpha_f^{max}}{r+d} \quad (5)$$

$$f_2^f = \frac{R\beta}{r+d} \quad (6)$$

where $\beta = \alpha_f^{max} + \theta_{eq} - \pi$; $R = r\left(\frac{\sin\alpha_f^{max} - (S+1)}{\sin\left(\alpha_f^{max} + \theta_{eq}\right)}\right)$

where R is the radius of curvature of the liquid meniscus.

Combining Equations (1), (2), (4)-(6) would yield the apparent contact angle of the yarn tow based on the equilibrium contact angle and geometrical parameters of the filaments. It should be noted that the magnitude of equilibrium contact angles of the filaments (θ_{eq}) can be calculated using advancing and receding contact angles [37], i.e.,

$$\theta_{eq} = \cos^{-1}\left(\frac{\Gamma_a\cos\theta_a + \Gamma_r\cos\theta_r}{\Gamma_a + \Gamma_r}\right) \quad (7)$$

where $\Gamma_a = \left(\frac{\sin^3\theta_a}{2-3\cos\theta_a+\cos^3\theta_a}\right)^{\frac{1}{3}}$ and $\Gamma_r = \left(\frac{\sin^3\theta_r}{2-3\cos\theta_r+\cos^3\theta_r}\right)^{\frac{1}{3}}$,

where θ_a and θ_r are the advancing and receding contact angles of the filament, respectively.

2.2. Apparent contact angle of woven fabric

X-ray micro-CT analysis has been utilized to gain insights into the 3D geometry of various woven fabrics, as illustrated in Fig. 1, highlighting the influence of the 'weave' on structural anisotropy. The weave of a fabric can be categorized as either reversible or irreversible [38], resulting in either similar or distinct surface topologies on the two faces of the fabric. Certain weave patterns may also produce a warp-rich or weft-rich topology[2] based on the two faces of a woven fabric. Thus, fabric surfaces will show different wetting behaviors when warp and weft yarns have dissimilar wettabilities. To address this complexity, a generalized multi-scale model has been developed to predict the apparent contact angle of woven fabric geometries, accommodating a diverse set of weaves and constituent yarns.

A vast array of weaves is currently employed in the production of woven fabrics [38,39], each capable of generating markedly different surface topologies based on the frequency of yarn interlacements and floats. Therefore, a methodology must be established to deconstruct a weave repeat into basic yarn configurations. Initially, a weave repeat can be represented as distinct yarn trajectories, with each yarn trajectory further decomposed into elementary yarn configurations. Figs. 3a and S1 present some of the most commonly used weaves alongside the individual yarn paths within them. Notably, each yarn path can be completely described using three fundamental yarn configurations (see Fig. 3b), but it is not necessary that all possible combinations of these configurations may exist in each type of weave. Intriguingly, a typical 2/2 twill weave inherently contains all the yarn configurations depicted in Fig. 3a, which collectively give rise to the formation of a composite solid–liquid–air interface.

To compute the apparent contact angle of the woven fabric (θ^*), the area fractions of liquid-warp/weft yarns (f_1^{wp}/ f_1^{wf}) and the area fraction of the liquid–air interface (f_2) must be calculated, extending the classical work of Cassie and Baxter [6], as shown below.

$$\cos\theta^* = f_1^{wp}\cos\theta_{wp}^* + f_1^{wf}\cos\theta_{wf}^* - f_2 \quad (8)$$

where, θ_{wp}^* and θ_{wf}^* are the apparent contact angles of the warp and weft yarns obtained using Equation (4).

In a hybrid woven fabric, where the warp-rich and weft-rich faces are composed of hydrophobic or hydrophilic yarns, $f_1^{(wp,WP)}$ denotes the area fraction of liquid–solid contact formed by the warp yarn (wp) on the warp-rich face (WP) of the fabric. Similarly, $f_1^{(wp,WF)}$ denotes the area

[2] A warp-rich or weft-rich topology describes the surface of a woven fabric where either the warp or the weft yarns are more prominently exposed than the other.

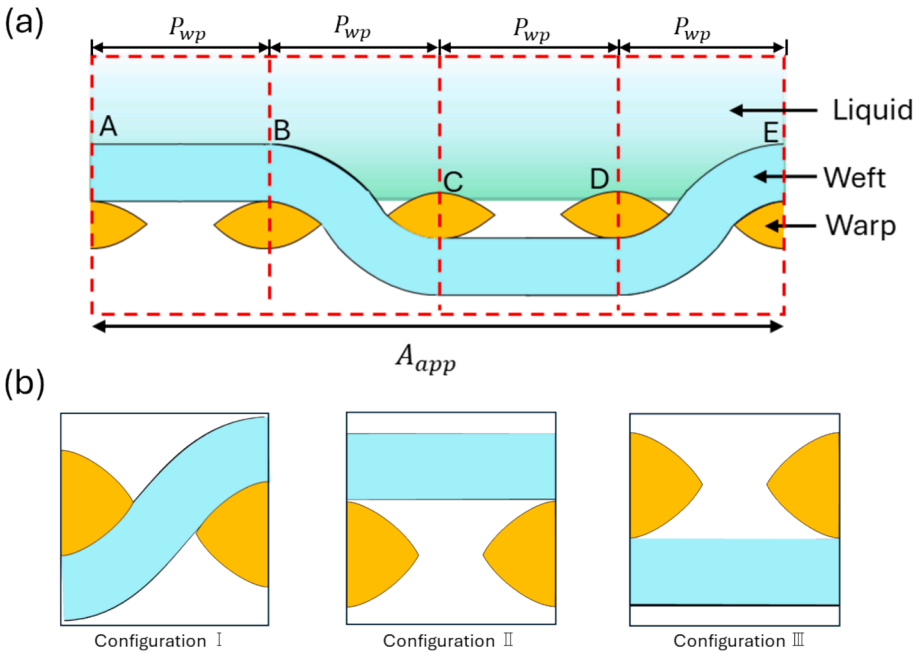

Fig. 3. (a) A typical 2/2 twill weave demonstrating (b) elementary yarn configurations, forming a composite liquid–solid–air interface across a single repeat unit. Considering a unit repeat perpendicular to the warp yarn, the region 'ABCDE' represents the total solid contact region made with the liquid droplet, while the apparent length of solid contact is $A_{app}(=4P_{wp})$, where P_{wp} is the distance between two consecutive warp threads.

fraction of liquid–solid contact formed by the warp yarn (*wp*) on the weft-rich face (*WF*) of the fabric. This dual-superscript format can be systematically extended to represent all combinations of yarn orientation (lower case, warp or weft) and fabric face (uppercase, warp-rich or weft-rich), allowing for a unified and explicit representation of face-specific wettability contributions.

As previously described, the composite solid–liquid-vapor interface developed on either warp or weft yarns can be systematically decomposed into interfaces associated with the three fundamental yarn configurations illustrated in Fig. 3b. Thus, f_1^{wp}, f_1^{wf} and f_2 can also be expressed as a combination of these three yarn configurations.

$$f_1^{wp} = \frac{1}{N}\sum_{i=1}^{3} n_i f_{1i}^{wp} \tag{9}$$

$$f_1^{wf} = \frac{1}{N}\sum_{i=1}^{3} n_i f_{1i}^{wf} \tag{10}$$

$$f_2 = \frac{1}{N}\sum_{i=1}^{3} n_i f_{2i} \tag{11}$$

where n_i is the number of i^{th}(=1,2,3) yarn configurations present in a weave repeat, N is the total number of yarn configurations present in the weave repeat (see Fig. S1), f_{1i}^{wp}, and f_{1i}^{wf} represent the area fraction of the liquid–solid contact formed by the warp and weft yarn in the i^{th} yarn configuration, and f_{2i} represents the area fraction of the liquid–air contact in the same configuration.

Therefore, an in-depth analysis of these elementary yarn configurations is essential for determining the components in Equations (9)-(11), and ultimately, θ^* from Equation (8). For simplicity, we consider the weft yarn as a cross-over yarn that passes over and under the two warp yarns. Similarly, the warp can be replaced by the weft when viewed from a opposite direction. Note that the subscripts '*wp*' and '*wf*' represent warp and weft yarns, respectively.

2.2.1. Configuration I

In configuration I, the repeat unit of plain weave (see Fig. S1) exemplifies a fundamental woven structure characterized by an alternating over-under pattern between orthogonal yarn sets. This alternating trajectory of yarns depicts a cross-over yarn, commonly referred to as 'yarn interlacement'. A typical formation of a solid–liquid–air interface in yarn configuration I, upon contact with the liquid, is depicted in Fig. 4.

Similar to the approach of Cassie and Baxter [6], consider a unit length of the grating in the direction normal to the plane of paper. Accrodingly, the total area of contact formed by the TCL can be delineated as 'ABCD' in a region normal to the plane of the fabric, while the apparent area corresponds to the inter-yarn distance. The lengths AB, BC and CD can be calculated using the lenticular geometry of the yarn-cross section. Fig. S2 identifies the fundamental attributes of the lenticular geometry, which can be defined as the combination of two inverted circular arcs, with the circular arc referred to as the parametric circle. Consequently, the components f_{11}^{wp}, f_{11}^{wf} and f_{21} can be expressed as:

$$f_{11}^{wp} = \frac{\mathrm{AB}}{P_{wp}} = \frac{d_{wp}\alpha_{wp}}{2P_{wp}} \tag{12}$$

$$f_{11}^{wf} = \frac{\mathrm{CD}}{P_{wp}} = \frac{(d_{wp}+2B_{wf})\alpha_{wf}}{2P_{wp}} \tag{13}$$

$$f_{21} = \frac{\mathrm{BC}}{P_{wp}} = 1 - \frac{(d_{wp}\sin\alpha_{wp} + (d_{wp}+2B_{wf})\sin\alpha_{wf})}{2P_{wp}} \tag{14}$$

where d_{wp} is the diameter of the parametric circle of the warp yarn, P_{wp} is the inter-yarn distance between warp yarns, B_{wf} is the minor diameter of the weft yarn, $\phi_{wp}\left(=\sin^{-1}\left(\frac{2A_{wp}B_{wp}}{A_{wp}^2+B_{wp}^2}\right)\right)$ is the angle of the lenticular arc, A_{wp} is the major diameter of warp yarn, B_{wp} is the minor diameter of warp yarn, $\alpha_{wp}(=\pi-\theta_{wp}^*)$, and $\alpha_{wf}(=\pi-\theta_{wf}^*)$ are the angles projected by the arc 'AB' and 'CD' at the center of the parametric circle. It should be noted that $f_{21} \leq 0$ would indicate a state of complete wetting.

2.2.2. Configuration II

A relatively smooth surface is formed when a yarn passes over two neighboring yarns in the orthogonal set, also known as 'face float,' in a

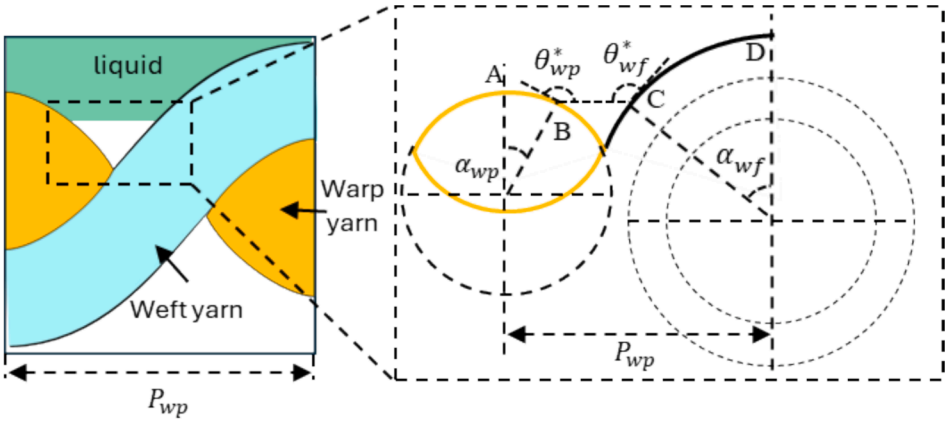

Fig. 4. Schematic illustrating a typical formation of a solid–liquid–air interface in yarn configuration I, upon contact with the liquid. On magnifying the liquid–solid contact, a yellow line represents the lenticular cross-section of the warp yarn, while the solid black line indicates the curved surface of the weft yarn where the meniscus rests. (For interpretation of the references to colour in this figure legend, the reader is referred to the web version of this article.)

woven structure, referred to as yarn configuration II in this work. A liquid droplet forms a flat TCL with the straight yarn, resulting in the same apparent and actual liquid–solid contact area, and is formed by one set of the yarns, as shown in Fig. 3b. Therefore, the corresponding components in Equations (9)-(11) can be recalculated as, $f_{12}^{wp} = 0, f_{12}^{wf} = 1$, and $f_{22} = 0$.

2.2.3. Configuration III

A 'back float' is formed when a yarn passes beneath two neighboring yarns in the orthogonal set. This yarn configuration, referred to as yarn configuration III in this work, creates a TCL resting on the lenticular pillars formed by the cross sections of exposed yarn, as shown in Fig. 3b. The geometric simplifications adopted herein for the TCL equilibrium are supported by previous studies that examined meniscus formation on surfaces composed of cylindrical and elliptical cross-sectional features [6,12,35,40,41]. While these studies illustrate plausible wetting outcomes, it is important to note that real rough surfaces are rarely as continuous or perfectly ordered as the idealized models considered in these references. However, such configurations provide valuable analogs for modeling TCL behavior in yarn or filament geometries, particularly in cases where direct experimental observation is inherently challenging. Nevertheless, it should be noted that the TCL may form two distinct geometric configurations with the pillars depending on its equilibrium position, as shown in Fig. 5. The equilibrium position of the TCL can be categorized into two cases: when $\alpha_{wp} \leq \phi_{wp}$ or $\alpha_{wp} > \phi_{wp}$.

Consequently, the expressions for f_{13}^{wp}, f_{13}^{wf} and f_{23} must be derived for each case.

Case I: $\alpha_{wp} \leq \phi_{wp}$

A larger θ^*_{wp} results in the equilibrium position of TCL on the upper arc of the lenticular cross-section as $\alpha_{wp} = \pi - \theta^*_{wp}$ as defined previously. This creates a relatively simpler geometry, similar to the work of Cassie and Baxter [6]. Therefore, the components in Equations (9)-(11) can be defined as (see Fig. S3 for details),

$$f_{13}^{wp} = \frac{d_{wp}\alpha_{wp}}{P_{wp}} \tag{15}$$

$$f_{13}^{wf} = 0 \tag{16}$$

$$f_{23} = 1 - \frac{(d_{wp}\sin\alpha_{wp})}{P_{wp}} \tag{17}$$

Case II: $\alpha_{wp} > \phi_{wp}$

A smaller θ^*_{wp} leads to a larger α_{wp}, resulting in a lower equilibrium position of the TCL. This scenario addresses the position of TCL on the lower arc of the lenticular cross-section. Such a geometry will result in a curved liquid meniscus; the radius of curvature of this meniscus, R', can be defined by the similar expression used in Equations (6) [35],

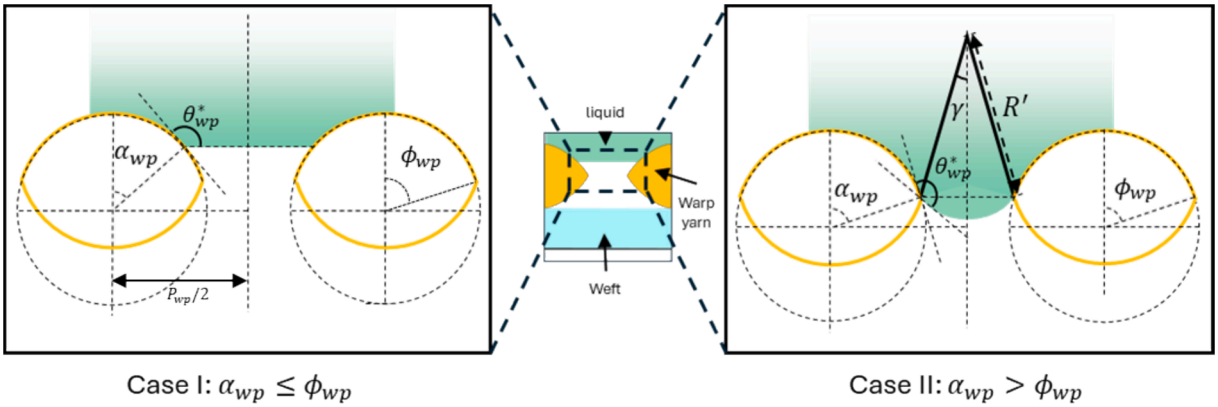

Fig. 5. Two distinct cases of the equilibrium position of TCL formed on magnifying yarn configuration III. Here, $\gamma\left(=\phi_{wp}+\theta^*_{wp}-\pi\right)$ is the half of the angle subtended by the curved meniscus arc on its center of curvature, θ^*_{wp} is the apparent contact angle of warp yarn, ϕ_{wp} is the angle of the lenticular arc of warp yarn, and R' is the radius of curvature of the meniscus.

$$R' = \frac{d_{wp}}{2}\left(\frac{\sin\alpha_{wp}^{max} - (J+1)}{\sin\left(\alpha_{wp}^{max} + \theta_{wp}^{*}\right)}\right) \tag{18}$$

where $J = \frac{P_{wp}}{d_{wp}} - 1$ and $\alpha_{wp}^{max} = \cos^{-1}\left[\frac{\sin\theta_{wp}^{*}\cos\theta_{wp}^{*} - \sin\theta_{wp}^{*}\sqrt{(J+1)^2 - \sin^2\theta_{wp}^{*}}}{J+1}\right]$.

Subsequently, the expression for f_{13}^{wp}, f_{13}^{wf} and f_{23} for this case can be given by:

$$f_{13}^{wp} = \frac{d_{wp}\phi_{wp}}{P_{wp}} \tag{19}$$

$$f_{13}^{wf} = 0 \tag{20}$$

$$f_{23} = \frac{2R'\gamma}{P_{wp}} \tag{21}$$

where $\gamma = \phi_{wp} + \theta_{wp}^{*} - \pi$.

Substituting the values of f_{1i}^{wp}, f_{1i}^{wf} and f_{2i} ($i = 1, 2, 3$) into Equations (9)-(11) can yield the apparent contact angle of a woven fabric using Equation (8). It should be noted that these equations can be applied to both faces of the fabric (top and bottom) and along both yarn directions (warp and weft). Currently, the unit cell of the fabric is considered orthogonal to the warp direction. In case of a fabric unit cell perpendicular to the weft direction, the '*wp*' and '*wf*' parameters are interchanged. For example, Equation (14) will be modified, as shown below.

$$f_{21} = 1 - \frac{(d_{wf}\sin\alpha_{wf} + (d_{wf} + 2B_{wp})\sin\alpha_{wp})}{2P_{wf}} \tag{22}$$

where P_{wf} is the distance between two weft yarns and d_{wf} is the parametric circle of the weft yarn.

Therefore, depending on the fabric's structural symmetry, the proposed analytical model may yield up to four distinct values for the apparent contact angle (e.g., two per face, accounting for directional anisotropy).

3. Materials and methods

3.1. Details of woven fabrics

The proposed model of the apparent contact angle of woven fabrics has been experimentally validated using three samples, namely F1 (carbon), F2 (polyester), and F3 (Kevlar/PTFE hybrid), featuring diverse morphological structures. Sample F1 was sourced from the Fuel Cell Store, Texas, USA, while sample F2 was fabricated in-house using 100 denier polyethylene terephthalate (PET) multifilament tows consisting of 36 filaments in both warp and weft directions. Sample F2 is a plain-woven fabric prepared on a Toyota LWT710 waterjet loom operated at a speed of 550 RPM, with a warp tension of 70 Kg and a weft insertion rate of 70 picks/inch. Sample F3, on the other hand, consists of a 2/2 twill fabric woven with Kevlar warp and polytetrafluoroethylene (PTFE) weft yarns, and was provided in-kind by the COMPLEXURF Research Lab at KU Leuven, Belgium. A detailed description of the preparation of sample F3 has been provided elsewhere [20]. The structural properties of these samples are listed in Table S1.

3.2. Measurement of yarn twist

The twist level of the yarns comprising the fabric was determined using a Paramount manual twist tester in accordance with ASTM D1423. Yarn specimens of varying lengths were carefully extracted from the fabric and mounted between the clamps of the tester. A minimum gauge length of 20 mm was maintained, and the yarns were manually untwisted by rotating the fixed clamp until the individual fibers or filaments became visibly parallel. To confirm complete untwisting, a needle was inserted through the fiber bundle to check for any residual twist. The total number of rotations was then divided by the gauge length to calculate the twist per unit length of the yarn.

3.3. Scanning electron microscopy (SEM) analysis

The surface morphology of the fabric samples and their constituent fibers was examined using SEM analysis. Specimens measuring 5 × 5 mm^2 were prepared from each sample and affixed to the stub of a Zeiss EVO 50 SEM (Carl Zeiss, Germany) using adhesive carbon tape. A conductive gold layer, approximately 10–15 nm thick, was deposited onto the samples using an Emitech K550X sputter coater (Labtech International). The prepared stub was subsequently mounted on the SEM stage, and imaging was performed at an accelerating voltage of 20 kV with a working distance of 12 mm. SEM micrographs were obtained at magnifications of 200× to assess fabric surface morphology and 5000× to investigate fiber surface characteristics.

3.4. X-ray micro-computed tomography (micro-CT) analysis

The structural characteristics of the woven fabric samples were extracted using X-ray micro-CT analysis. Here, X-rays were directed onto the sample stage from a tungsten target, with optimal source voltage and current settings, generating datasets comprising 1500 –1800 images per sample. The scanning parameters used for X-ray micro-CT analysis are detailed in Table S2. Reconstruction of the acquired data involved corrections for beam hardening, defect pixel masking, and ring artefact reduction, employing ZEISS OptiRecon and NRecon® (Bruker, Belgium) software to enhance dataset quality for further processing. Noise reduction was performed using either a Box filter or a non-local mean filter, followed by thresholding via Otsu's algorithm to obtain a binarized dataset [42].

The processed dataset was analyzed using GeoDict® (Math2Market) to extract key structural parameters of the fabric, such as yarn packing fraction and major and minor yarn diameters. In addition, various construction parameters, including ends per inch (EPI), picks per inch (PPI), and weave pattern, were extracted using X-ray microCT analysis and corroborated with an optical microscope. By employing a simple pixel-counting algorithm, the yarn packing fraction was determined by computing the ratio of fiber-occupied pixels to the total pixels within the yarn cross-section. The major and minor yarn diameters were measured using the open-source software ImageJ®, applied to cross-sectional images of the fabric obtained via X-ray micro-CT, as illustrated in Fig. S4.

3.5. Wettability analysis

3.5.1. Single fiber contact angle measurement

The dynamic contact angle of a single fiber was measured using Wilhelmy's method with the K100SF tensiometer [43]. According to this method, the fiber was mounted on a sample holder, while the stage containing the liquid container was moved vertically (up and down) at a controlled speed of 1 mm/min. This ensured consistent immersion and withdrawal of the fiber through the liquid, thereby minimizing experimental errors.

Initially, the perimeter of the fiber was determined by immersing it in n-hexane, a low surface tension liquid providing a contact angle of ~ 0°. The recorded capillary force in n-hexane was used to calculate the perimeter of the fiber, assuming uniformity along its length. After establishing the perimeter, the fiber was immersed in deionized water to measure the capillary forces. The values of the perimeter and the contact angle of the fiber with water were calculated using Wilhelmy's equation [44], i.e., $F_f = C_w\gamma_{LV}\cos\theta_d$, where F_f is the measured force, C_w is the wetted perimeter of the fiber, γ_{LV} is the liquid–vapor surface tension and θ_d is the dynamic contact angle (advancing or receding, depending on the stage motion direction). It should be noted that the experiments

were conducted under controlled conditions, with regulated temperature (~ 25 °C) and humidity (~ 65 %) to maintain a constant surface tension of the liquid. In addition, the setup included a vibration-free table and a protective cabinet to minimize external disturbances.

3.5.2. Apparent contact angle measurement

The wetting behavior of samples F1 and F2 was analyzed using a Dataphysics 15EC optical contact angle measuring system. The apparent contact angle of the samples was measured using a 10 μL droplet of deionized water dispensed at a 2 μl/s dosing rate using a 25-gauge needle mounted to a Hamilton 100 μL glass syringe. Subsequently, five images of each sample were analyzed using ImageJ® software [45] to determine the contact angles at different viewing orientations, which were achieved using a custom-built rotating stage, as shown in Fig. S5. Here, a 10 μL droplet was dispensed at 2 μL/s using the same needle parameters as those employed for the apparent contact angle measurements. The droplet was placed on the rotating stage mounted on the Dataphysics 15EC, and images were captured at 45° intervals. It should be noted that the advancing and receding contact angles for Sample F3 were taken from the literature [20] and measured using a Dataphysics OCA 50. In addition, an automated in-house developed instrument described in a previous publication [46] was utilized for the measurement of roll-off angles. All measurements were performed in standard laboratory conditions at a temperature of 25 ± 2 °C and a relative humidity of 65 ± 2 %.

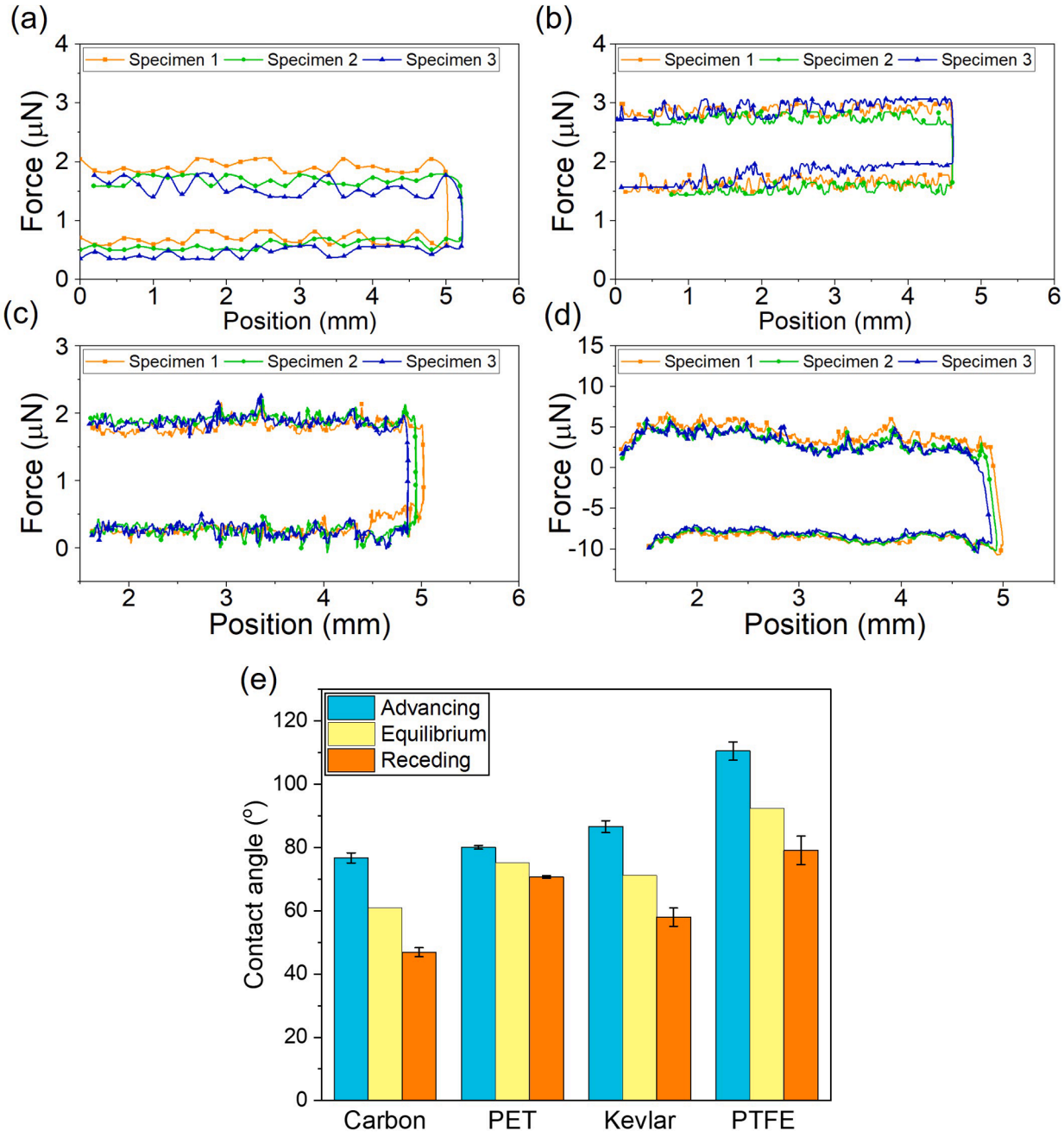

Fig. 6. Measurement of adhesion forces exerted during the advancing and receding cycles in case of (a) carbon, (b) PET (c) Kevlar [20] and (d) PTFE filaments [20] using a KS100F tensiometer. (e) Measurement of dynamic contact angles (advancing and receding) along with the equilibrium contact angle calculated using Equation (7). The dynamic contact angles for Kevlar and PTFE were obtained from the literature [20].

4. Results and discussion

4.1. Wettability at micro-scale (filaments)

Deciphering the hierarchical morphology of woven fabrics allows their systematic unfolding into yarns, which, in turn, consist of individual fibers or filaments – fundamental building blocks that govern interfacial interactions at the microscale [25,47,48]. Irrefutably, the spatial organization and surface chemistry of these constituent filaments in a yarn significantly influence the wettability characteristics of hydrophobic fibrous assemblies [49]. Conventionally, the wettability of textile surfaces is assessed through the equilibrium contact angle formed between a sessile water droplet and the planar substrate [44]. However, applying such methodology to cylindrical geometries, such as individual fibers, presents significant challenges. The droplet profile becomes distorted due to the interplay between Laplace pressure and gravitational forces, especially when the droplet is placed on a horizontally oriented filament [50,51]. To circumvent such a limitation, the Wilhelmy method is implemented through a tensiometer to characterize fiber wettability. This technique involves quantifying the dynamic contact angles (advancing and receding) by immersing and withdrawing a single filament from a liquid interface [44,52,53].

Fig. 6a-d shows the force profile experienced by the fiber as the stage containing the liquid container moves upward (advancing cycle) and downward (receding cycle), thereby successively immersing and withdrawing fiber into and out of the liquid. According to Wilhelmy's equation, the measured force linearly varies with the wetted perimeter (C_w) and the cosine of the dynamic contact angle (θ_d). As demonstrated in Fig. 6a and b, this correlation is corroborated by the experimental observations wherein PET filaments, with an average diameter of 17.4 μm, exhibit higher capillary forces than carbon fibers with a diameter of 9 μm. It must be noted that the difference between the average forces during the advancing and receding cycles is 1.3 μN for carbon fibers and 1.1 μN for PET filaments, indicating a greater disparity between the wetting and dewetting energies of the carbon fibers. Kevlar filaments, on the other hand, possess a higher force despite having a substantially smaller perimeter (~43 μm), whereas PTFE filaments, even though they exhibit significantly larger perimeters (~270–320 μm), display a negative force during immersion [20]. Here, a negative force implies a very high advancing contact angle, a result consistent with the values observed in Fig. 6e. Conversely, during the withdrawal phase, PTFE filaments exhibit greater capillary forces than Kevlar, attributed to the enhanced liquid–solid interfacial area registered by their large perimeter.

Furthermore, the force–position curves obtained from Wilhelmy's analysis typically display oscillatory behavior, demonstrating a 'stick–slip' mechanism resulting from the intermittent pinning of the TCL [20,53,54]. This dynamic behavior is frequently encountered during single-fiber wetting measurements and is further exacerbated by microscale surface irregularities [55–58]. Nevertheless, the tensiometry data in Fig. 6a-d have been a cornerstone in computing the average advancing and receding contact angles of all the constituent materials of samples F1, F2, and F3, as summarized in Fig. 6e. Although the advancing contact angles of PET (80°) and carbon fiber (77°) are relatively similar, their receding angles differ substantially, with PET exhibiting a receding contact angle of 71°, whereas that of carbon fiber is significantly lower at 47°. The obtained values are consistent with those reported in the literature [54,59].

In addition, the average values of dynamic contact angles also manifest an important aspect of fiber wetting behavior, i.e., contact angle hysteresis that arises as a result of the energy gained as the liquid wets an initially dry solid surface, exceeding the work of adhesion needed to detach the liquid [60]. This energy difference is further amplified by the roughness of the wetted surface, resulting in a higher contact angle hysteresis [60]. Notably, carbon fibers and Kevlar filaments display rougher surface morphologies than PET filaments, as depicted via SEM micrographs (see Fig. 7). While prominent surface irregularities in the form of striations are evident in carbon fibers (Fig. 7a1), the surface heterogeneities of Kevlar filaments appear subtly in the form of nodules and indentations, as indicated in Fig. 7c1 via dotted white circles. Such features have also been previously reported in the literature [61]. Meanwhile, the PTFE filament, though having a smoother surface, has a twisted architecture, which likely contributes to the pinning of the TCL during the wetting-dewetting cycle [20]. This structural feature of PTFE may account for the significantly higher contact angle hysteresis observed in comparison to the other filaments, as illustrated in Fig. 6e. Contact angle hysteresis is the lowest for the PET filaments owing to their smooth surface morphology, as depicted in Fig. 6e. Note that Equation (7) computes the equilibrium contact angle using an advancing–receding weighted average formulation, as commonly applied in wetting models. Given that the contact angles were measured using the Wilhelmy plate method under continuous immersion and withdrawal, the influence of time-dependent wetting transitions is minimized, and the obtained values are representative of a steady-state response. While time-dependent phenomena may become significant in highly dynamic environments or over extended timescales, incorporating such effects remains a promising direction for future research.

4.2. Wettability at meso (yarn) and macro (fabric) scales

Yarns, which form the mesoscale morphological features of hierarchical woven structures, are typically composed of parallel or twisted bundles of filaments whose wetting behavior is fundamentally governed by their internal filament arrangement [49,62]. The wettability of yarns is generally assessed through Wilhelmy's method, as described in the preceding section, or via analysis of their wicking behavior, which arises due to microscopic capillaries formed within the yarn structure [63,64]. In both approaches, yarns are vertically suspended during measurement, which deviates from their actual in-plane alignment and mechanical constraints within a woven fabric, thereby limiting the representativeness of such analyses. Therefore, we predicted the apparent contact angle of the yarn by modeling it as a parallel array of cylindrical filaments with a water droplet positioned on top of the filament surface [25].

The pioneering work of Cassie and Baxter [6] on droplets resting on parallel cylinders provides the basis for this approach, where the area fractions of the solid/liquid interface, $f_1 (= r(\pi - \theta_{eq})/(r + d))$ and the liquid/air interface, $f_2 (= 1 - r\sin\theta_{eq}/(r + d))$ can be defined as functions of spacing ratio, $S (= d/r)$. In this work, the yarn packing is assumed to follow a hexagonal close-packing geometry, S has been related to the fiber volume fraction V_f via Equation (2), following the methodology outlined by Piggott [65]. Consequently, it can be hypothesized that the wettability of multifilament yarns with nominal or no twist is influenced by both the packing density of the filaments and the intrinsic equilibrium contact angle of the fiber. Fig. 8 displays representative cross-sectional micrographs of yarns from samples F1, F2, and F3, highlighting notable variations in filament spacing and packing fractions. The PTFE yarn displays a markedly different morphology, characterized by a partially solid structure, which is significantly different from idealized hexagonal filament packing and with an exceptionally high fiber volume fraction, as shown in Table S1. This highly compact configuration imparts a smoother surface appearance to the PTFE yarns, a feature also discernible in Fig. 7d and 7d1. Therefore, the PTFE yarn is assumed to be a solid filament for modeling purposes. This approximation is also consistent with the modeling approach used by Lu et al. [34] and supports the applicability of the model despite deviations from ideal filament packing. Nevertheless, the other yarns exhibit lenticular cross-sections, with observable differences between the major and minor diameters, as illustrated in Fig. 8 and Table S1.

As aforementioned, the realistic fabric geometry positions the yarns

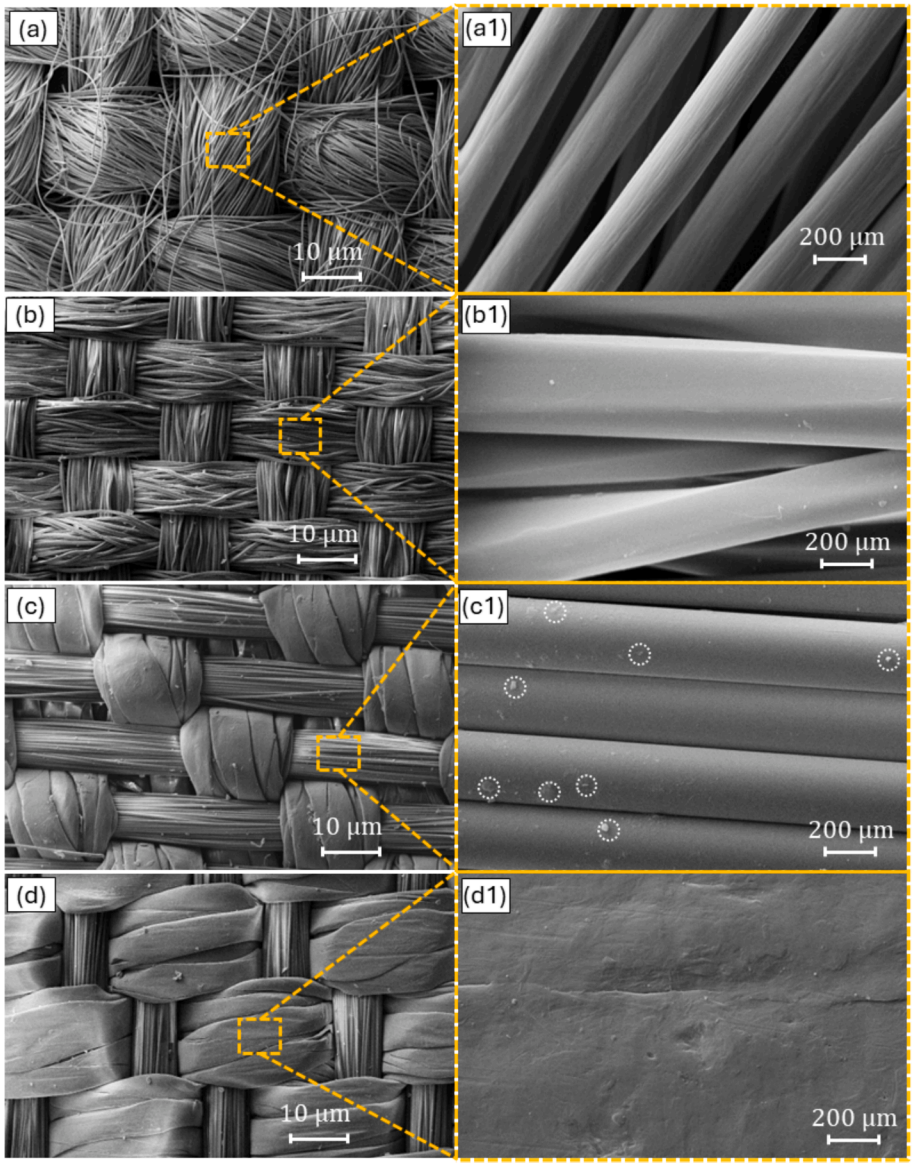

Fig. 7. SEM images of samples (a) F1, (b) F2, (c) F3- Kevlar face and (d) F3-PTFE face at a magnification of 200× showing the structure of the fabric with insets (a1), (b1), (c1) and (d1) at a magnification of 5000× showing a closer view of the fiber surface. The dotted white circles in (c1) mark the subtle nodules and indentations on the surface of Kevlar filaments.

predominantly in-plane; this parallel arrangement of filaments consistently promotes the anisotropic deformation of water droplets. Princen [66] and Duprat et al. [67] revealed that droplets placed on aligned cylindrical arrays tend to spread preferentially along the filament axis, forming elongated liquid bridges between adjacent cylinders. Such directional spreading implicitly assumes a continuous and uninterrupted surface – an assumption rarely valid in woven fabrics, where the surface of one yarn set is periodically disrupted by the orthogonal interlacement of crossing yarns, as illustrated in Figs. 1 and 7. These interruptions may alter the direction of the liquid flow, resulting in (an)isotropic spreading patterns and localized accumulation of liquid at yarn cross-overs. Accordingly, (an)isotropy in droplet behavior has been assessed by determining apparent contact angles on woven samples from multiple viewing orientations. Following the determination of apparent contact angles of the woven samples in multiple directions, a comparison between predicted and experimental results has been made in both the warp and weft directions. A representative illustration of apparent contact angles in warp-rich and weft-rich regions, measured along the warp and weft directions in a hybrid fabric, is shown in Fig. 9a.

Fig. 9b illustrates the variation in apparent contact angles of woven samples across the multiple viewing orientations. As anticipated, sample F1 is a square fabric composed of identical warp and weft yarns with the same inter-yarn spacing in both directions, showing insignificant variation in the apparent contact angle across multiple viewing orientations. In contrast, fabric architectures possessing heterogeneity, such as samples F2 and F3, induced localized anisotropic spreading, leading to variations in apparent contact angles depending on the observational direction, as shown in Fig. 9b. Sample F2 exhibits moderate structural heterogeneity, introduced by varying the spacing between warp and weft yarns. On the other hand, sample F3 demonstrates a significantly more complex heterogeneity due to differences in weave structure and yarn composition (see Fig. 7c and 7d). Specifically, the 2/1 twill weave of sample F3 generates distinct surface morphologies on opposite fabric faces: one face predominantly exposes the warp yarns (Kevlar), whereas the opposite face primarily reveals the weft yarns (PTFE), as evident in Fig. 7c and 7d. Furthermore, using two dissimilar yarn types with contrasting wetting characteristics amplifies the surface heterogeneity, promoting more pronounced directional deformation of water droplets

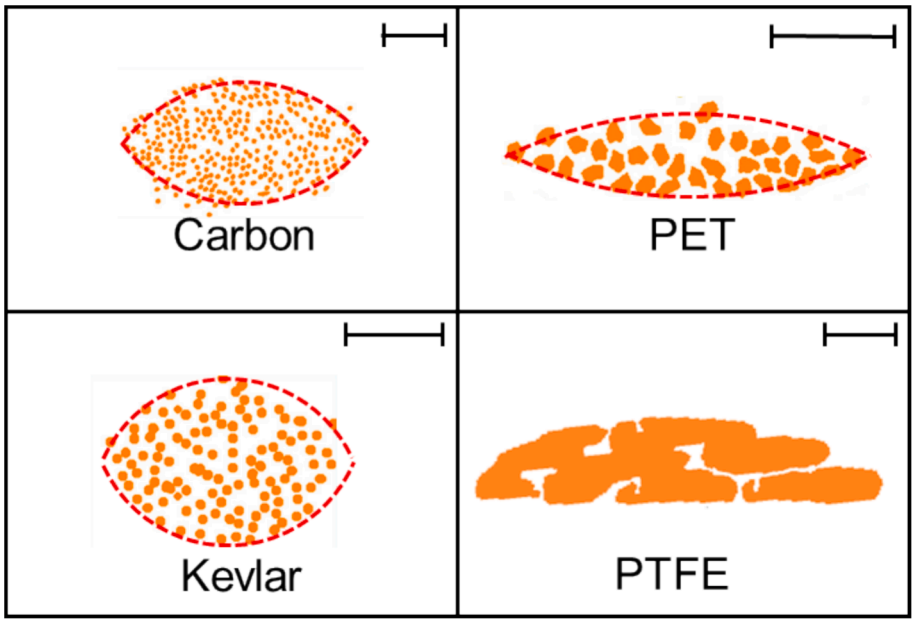

Fig. 8. Yarn cross-sections extracted from microCT analysis. The scale represents a length of 100 μm.

[20].

Another measure of contact angle hysteresis is the roll-off angle, which denotes the tilt angle at which a water droplet begins to slide off the surface [68]. High contact angle hysteresis inhibits droplet mobility, resulting in the so-called 'rose petal effect', characterized by an apparent contact angle of 150° [69]. Fig. S6 depicts the pinning of the droplet on the surfaces of the woven fabric samples, showing that the droplet remains firmly adhered when the surface is rotated to 90° or even upside down. Further, the contact angle hysteresis is much larger in the Wenzel state than in the Cassie-Baxter state [70]. Transition of metastable Cassie-Baxter state to Wenzel or wetting state has been measured and illustrated in Fig. S7. Sample F2 exhibited the fastest wetting transition, completing in ~ 6 min, whereas the remaining samples generally required over 20 min to become fully wetted. The tightly packed architecture of Sample F2 and its low warp yarn separation ratio (see Table S1) contribute to reduced fabric porosity. Such structural features, in combination with the moderately hydrophilic nature of polyester filament facilitate faster droplet penetration and accelerate the transition from the Cassie–Baxter to the Wenzel state in sample F2. In future studies, we aim to integrate high-speed, time-resolved contact angle measurements during dynamic wetting transitions similar to our earlier work on curved substrates [71]. This will allow us to capture transient interfacial states and better quantify the kinetics of wetting regime shifts. Such data will not only enhance the fidelity of model validation but also provide deeper mechanistic insights into how structural features such as yarn crimp, yarn spacing, filament orientation, and surface roughness govern the evolution of wetting behavior over time.

Further, the apparent contact angles of samples F1, F2, and F3 in all four defined directions (see Fig. 9a) were compared using both predicted and experimental measurements, as illustrated in Fig. 10. The results clearly indicate a range of wetting behaviors, from strongly hydrophobic to weakly hydrophobic responses. Sample F1 exhibits the highest apparent contact angle of 132 ± 8° when viewed from $\theta^*_{(wp,WP)}$, while sample F3 shows the lowest value of 102 ± 9°, when observed from $\theta^*_{(wf,WP)}$. In general, there are insignificant differences between the apparent contact angles of woven samples F1 and F2 when measured from four different directions. On the other hand, sample F3 demonstrates distinct values for each of the four contact angles owing to its pronounced structural heterogeneity. The lowest contact angle associated with $\theta^*_{(wf,WP)}$ can be attributed to a higher solid/liquid interfacial area contribution from the weakly hydrophobic Kevlar yarns. On the other hand, the '*WF*' face of sample F3, which exhibits a higher content of hydrophobic PTFE yarns, yields elevated contact angles ($\theta^*_{(wp,WF)}$, $\theta^*_{(wf,WF)}$). Nevertheless, a reasonable agreement between theory and experiments has been observed across all samples, as shown in Fig. 10.

In general, the predicted results underestimate the measured values of the apparent contact angle, plausibly due to its inability to account for the individual or combined effects of microstructural roughness, air entrapment, fabric anisotropy, variation in local yarn spacing, localized liquid accumulation at yarn cross-overs, and pinning of the three-phase contact line (TCL). For instance, the predictive model has not accounted for the microstructural roughness inherent to carbon and Kevlar filaments; incorporating such surface characteristics would likely have resulted in higher apparent contact angles, consistent with roughness-enhanced hydrophobicity, as described by the Cassie–Baxter model [6]. Similarly, incorporating the twist in PET and PTFE filaments into the theoretical model may have reduced the effective area available for droplet contact, potentially resulting in an increase in the apparent contact angle of the fabric. Nevertheless, the predictive model effectively captured the structural heterogeneity of sample F3, reflecting the trend in apparent contact angles when measured from four different directions.

One of the key aspects of integrating micro-, meso-, and macro-scale structural features of woven fabrics with the equilibrium contact angle of individual fibers lies in its potential to accelerate the development of a unified design principle and scientific framework for controlling wettability characteristics – ultimately enabling the realization of superhydrophobic behavior. The theoretical framework thus plays a pivotal role in achieving the desired apparent contact angle by systematically modulating key fiber-, yarn-, and structure-related parameters [25]. Accordingly, a virtual experiment involving key yarn- and fabric-structure parameters, along with the equilibrium contact angle of individual fibers, was systematically optimized to achieve superhydrophobicity in the woven fabric, with a focus on maximizing the apparent contact angle. Further details on the virtual experiment can be found in the supplementary information.

The yarn packing fraction – a dimensionless figure of merit that quantifies how dense fibers are packed within a yarn's cross-section – along with the fiber equilibrium contact angle governs the apparent contact angle of the yarn, as illustrated in Fig. 11a. In general, a yarn

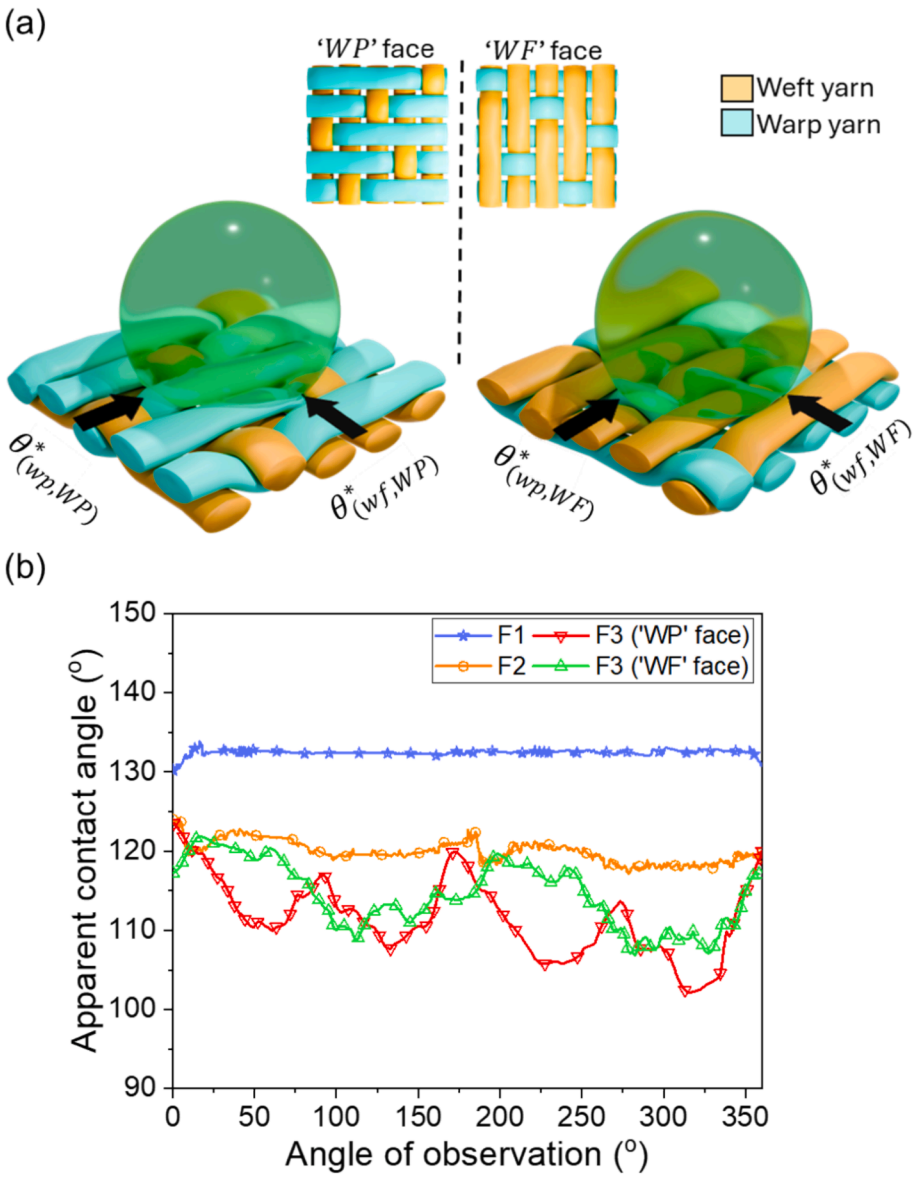

Fig. 9. (a) Schematic representing determination of the apparent contact angles in warp-rich and weft-rich regions, measured along the warp and weft directions in a hybrid fabric. (b) Variation of the apparent contact angles in woven fabric samples in multiple viewing directions. Here, the notations '*WP*' and '*WF*' denote the warp and weft-rich faces of the fabric, while '*wp*' and '*wf*' indicate the direction of observation, parallel to the warp and weft yarns, respectively. For example, $\theta^*_{(wp,WP)}$ corresponds to the apparent contact angle when observed along the warp direction on the warp-rich surface of the fabric. The variation of the apparent contact angle with viewing direction for sample F3 was obtained from the literature [20].

with a low packing fraction represents a loosely packed structure containing significant air voids, thereby promoting a Cassie-Baxter wetting regime. A combinatorial strategy using moderate yarn packing fractions and weakly hydrophobic constituent fibers can induce a significant hydrophobic effect in yarns. Particularly, for yarns with a packing fraction of 0.6 or higher, the predicted apparent contact angle converges and shows minimal variation, especially when they are hydrophilic (see Fig. 11a). However, yarn float length exhibited an insignificant effect on the apparent contact angle of the woven fabrics, even across a range of yarn-level apparent contact angles (see Fig. S8a). Similar insignificant effects of yarn float length, in combination with lower values of the yarn separation ratio, have been observed on the apparent contact angle of the woven fabric, as depicted in Fig. S8b. Nevertheless, as anticipated, superhydrophobicity in a woven fabric can be attained by targeting a large yarn separation ratio and minimal yarn float length.

Combining a moderate to high yarn separation ratio (4–5) with a moderate apparent yarn contact angle (100°-120°) can also result in superhydrophobic behavior in woven fabrics through air entrapment [6], as depicted in Fig. 11b. A higher yarn separation ratio corresponds to increased openness within the fabric structure, leading to larger trapped air pockets at the liquid–solid interface. This increased air fraction enhances the liquid–air interfacial area beneath the droplet, raising the apparent fabric contact angle. Notably, in the regime of moderate hydrophobicity – commonly observed with water, where Young's contact angles typically do not exceed 120° – the Cassie-Baxter state involving air entrapment is often metastable [70]. To create a superhydrophobic surface by minimizing droplet adhesion, it is essential to reduce the roll-off angle, which can be analyzed using existing models proposed by Furmidge [72], Kawasaki [73] or Extrand and Gent [74]. Choi et al. [75] built upon the work of Extrand and Gent [74] to establish a relation between roll-off angle and contact angle hysteresis by introducing differential changes in the liquid–solid area fractions (ψ) during

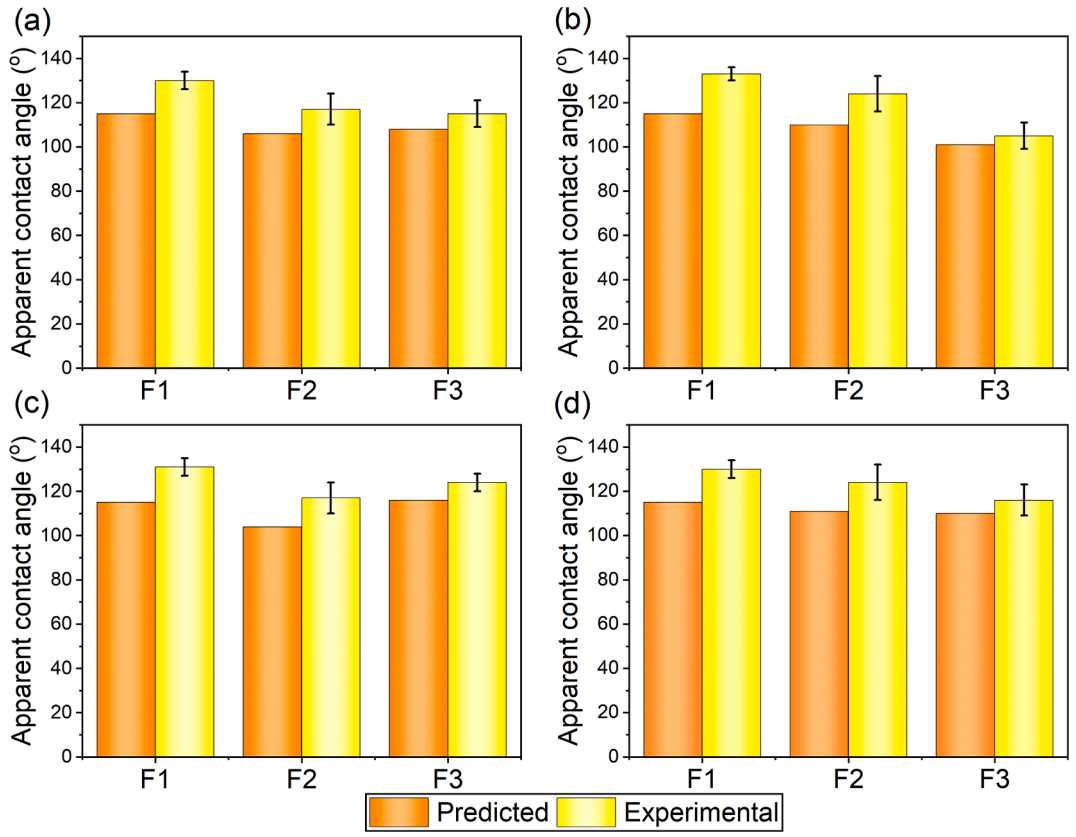

Fig. 10. Comparison between the predicted and experimental apparent contact angle values for (a) $\theta^*_{(wp,WP)}$,(b) $\theta^*_{(wf,WP)}$, (c) $\theta^*_{(wp,WF)}$ and (d) $\theta^*_{(wf,WF)}$. Here, the notations '*WP*' and '*WF*' denote the warp and weft-rich faces of the fabric, while '*wp*' and '*wf*' indicate the direction of observation, parallel to the warp and weft yarns, respectively. For example, $\theta^*_{(wp,WP)}$ corresponds to the apparent contact angle when observed along the warp direction on the warp-rich surface of the fabric. The experimental values of the apparent contact angles for sample F3 were obtained from Ref. [20].

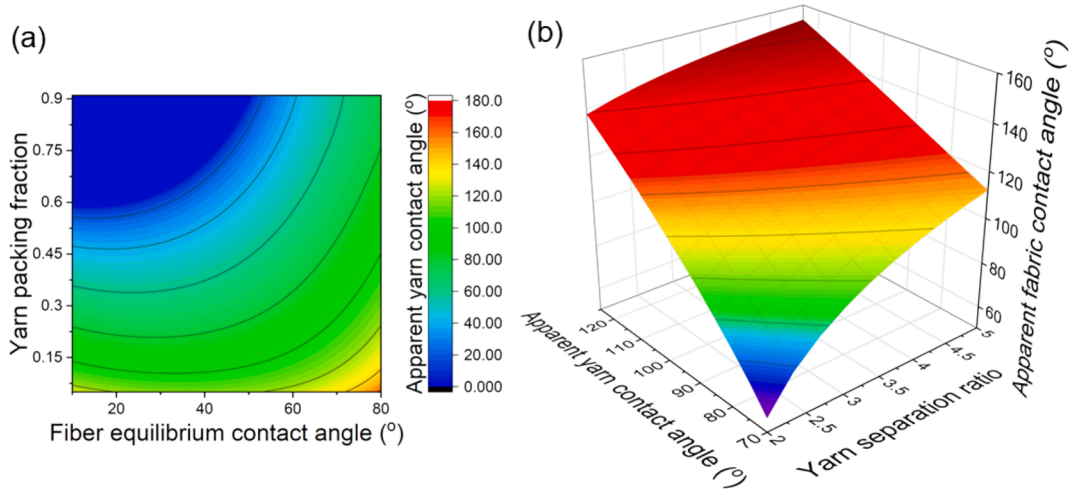

Fig. 11. Parametric analysis illustrating the influence of fiber-level and yarn-level parameters on wettability behavior. (a) Contour plot showing the variation of apparent yarn contact angle as a function of fiber equilibrium contact angle and yarn packing fraction. (b) Surface plot demonstrating the relationship between the apparent fabric contact angle, the apparent yarn contact angle and the yarn separation ratio in a plain-woven fabric. Here, Figure (b) is plotted by fixing yarn packing fraction ($V_f = 0.36$), yarn major diameter ($A = 280$ μm) and yarn minor diameter ($B = 70$ μm). Here, the yarn separation ratio denotes the ratio of the inter-yarn spacing to the yarn's major diameter.

droplet displacement, i.e., $\psi_{d,adv}$ for advancing and $\psi_{d,rec}$ for receding motion. The roll-off angle, ω can be calculated as $\sin\omega \approx \left(2\gamma_{LV}\overline{D}_{TCL}((r_\psi\psi_{d,rec} - r_\psi\psi_{d,adv})\cos\theta^*_y + (\psi_{d,rec} - \psi_{d,adv})\cos\theta_{LV})/\pi\rho gV\right)$, where $\overline{D}_{TCL}\left(\approx 2\cos\left(\theta^* - \frac{\pi}{2}\right)\left(\frac{3V}{\pi(2-3\cos\theta^*+\cos^3\theta^*)}\right)^{1/3}\right)$ is the average diameter of the TCL, γ_{LV} is the surface tension of the liquid, ρ is the density of water, g is the acceleration due to gravity, V is the volume of the droplet, θ_{LV} is the equilibrium contact angle between air and the liquid and r_ψ is the roughness of the wetted solid (fabric)–liquid interface. Based on the analysis of Choi et al. [75] θ_{LV} can be considered as 0°,

as the presence of disconnected pore spaces within the woven structure may cause the receding droplet to leave behind a thin liquid film over the underlying air pockets. Fig. S9 illustrates the sensitivity of the roll-off angle to variations in the apparent yarn contact angle. A roll-off angle below 5° can be achieved in combination with apparent fabric contact angles exceeding 150° thereby satisfying the dual requirements for superhydrophobicity by minimizing both $\psi_{d,adv}$ and $\psi_{d,rec}$. Future work should focus on deriving explicit expressions for $\psi_{d,adv}$ and $\psi_{d,rec}$, based on fabric geometry to establish a comprehensive roadmap for optimizing design parameters aimed at achieving self-cleaning and low-adhesion characteristics. In addition, future refinements of the model could also incorporate the twisted architecture of individual PTFE filaments as an additional microscale roughness factor, which may further improve the prediction of contact angle hysteresis of the woven fabric.

5. Conclusion

This work has successfully developed a comprehensive theoretical framework for dealing with the wetting behavior of woven fabrics by correlating the apparent water contact angle with the multi-scale structural hierarchy and the equilibrium contact angle of the filament. Leveraging the principles of multi-scale structural hierarchy, we successfully predicted the apparent contact angle of three distinct woven fabrics comprising polyester, a hybrid of Kevlar/ PTFE, and carbon by accounting for micro-, meso- and macro-scale topological features from four different directions. Although a satisfactory agreement between theory and experiments has been observed across all samples, the measured apparent contact angle values tend to overestimate the predicted results, plausibly due to inherent variations in micro- and meso-scale features. Further, the assessment of (an)isotropy in droplet behavior, based on apparent contact angles measured from multiple viewing directions, revealed that fabric architectures (polyester and hybrid of Kevlar/ PTFE) exhibit heterogeneity-induced localized anisotropic spreading. The polyester-based woven sample possessed the fastest wetting transition among all tested samples, primarily due to the moderately hydrophilic nature of the polyester filament and lower porosity.

Our findings underpin the fundamental insights into the wetting behavior of woven fabrics through virtual experiments that optimize yarn- and fabric-structural parameters, and the equilibrium contact angle of individual fibers to achieve superhydrophobicity. Targeting the superhydrophobic effect in a woven fabric can be achieved through a large yarn separation ratio, a moderate apparent yarn contact angle, and minimal yarn float length. While this study establishes a foundational framework for the geometric design of woven fabrics with tailored wetting properties, it is important to recognize the current limitations of the model. Specifically, it does not fully capture the wetting behavior of staple yarns, which are characterized by higher surface roughness, fiber misalignment, and internal filament reorientation – factors that affect both yarn packing and surface topology. Furthermore, it is currently applicable to fabrics exhibiting Cassie–Baxter-type wetting and does not explicitly address transitions to the Wenzel state, time-dependent wetting dynamics, or consider the influence of surface coatings and chemical treatments that alter interfacial energy. To overcome these limitations and broaden the model's applicability, future work should focus on incorporating the structural properties of short-staple yarns, filament-level surface roughness, yarn-level curvature (crimp), and the effects of yarn twist. In addition, extending the framework to capture transitions between Cassie–Baxter and Wenzel wetting regimes and modeling capillary-driven fluid imbibition would enable a more comprehensive understanding of static and dynamic wetting in complex fabric systems. Integrating parameters such as the realistic arrangement of filaments within the yarn, varying filament cross-sections, and filament surface roughness would further enhance model precision.

Nomenclature

α_f^{max}	Maximum inclination angle formed by the liquid meniscus on the filaments
α_{wp}^{max}	Maximum inclination angle formed by the liquid meniscus on the warp yarns
α_f	Inclination angle formed by the liquid meniscus on the filaments
α_{wp}	Inclination angle formed by the liquid meniscus on the warp yarns
α_{wf}	Inclination angle formed by the liquid meniscus on the weft yarns
γ_{LV}	Surface tension of the liquid
δ	Acute angle between the two neighbouring filaments
κ	Helical angle (Twist angle) of the fibers
ρ	Density of water
θ_{eq}	Equilibrium contact angle of a filament
θ_y^*	Apparent contact angle of yarn
θ_{LV}	Equilibrium contact angle between air and the liquid
θ_a	Advancing contact angle of a filament
θ_d	Dynamic contact angle
θ_r	Receding contact angle of a filament
θ^*	Apparent contact angle of the woven fabric
θ_{eq}^{wp}	Equilibrium contact angle of warp yarn
θ_a^{wp}	Advancing contact angle of warp yarn
θ_r^{wp}	Receding contact angle of warp yarn
θ_{eq}^{wf}	Equilibrium contact angle of weft yarn
θ_a^{wf}	Advancing contact angle of the weft yarn
θ_r^{wf}	Receding contact angle of the weft yarn
$\theta_{(wp,WP)}^*$	Apparent contact angle on the warp-rich face (warp-axis view)
$\theta_{(wf,WP)}^*$	Apparent contact angle on the warp-rich face (weft-axis view)
$\theta_{(wp,WF)}^*$	Apparent contact angle on the weft-rich face (warp-axis view)
$\theta_{(wf,WF)}^*$	Apparent contact angle on the weft-rich face (weft-axis view)
θ_{wp}^*	Apparent contact angle of a warp yarn
θ_{wf}^*	Apparent contact angle of a weft yarn
ϕ_{wp}	Angle of lenticular arc in warp yarn
$\psi_{d,adv}$	Liquid-solid area fraction during droplet displacement in advancing mode
$\psi_{d,rec}$	Liquid-solid area fraction during droplet displacement in receding mode
ω	Roll-off angle
A_{wp}	Major diameter of the warp yarn
B_{wp}	Minor diameter of the warp yarn
B_{wf}	Minor diameter of the weft yarn
C_w	Wetted perimeter of the fiber
d	Half of the edge-to-edge distance between two consecutive filaments
d_{wp}	Diameter of the parametric circle of the warp yarn
d_{wf}	Diameter of the parametric circle of the weft yarn
D_{wf}	Diameter of the weft yarn curvature in its longitudinal plane
$\overline{D_{TCL}}$	Average diameter of the three-phase contact line
D_y	Yarn diameter
E	Empirical parameter
$f_1^{(wp,WP)}$	Area fraction of liquid-solid contact (warp yarn) on the warp face
$f_1^{(wp,WF)}$	Area fraction of liquid-solid contact (warp yarn) on the weft face
$f_1^{(wf,WP)}$	Area fraction of liquid-solid contact (weft yarn) on the warp face
$f_1^{(wf,WF)}$	Area fraction of liquid-solid contact (weft yarn) on the weft face
f_2^{WP}	Area fraction of liquid-air contact on the warp face
f_2^{WF}	Area fraction of liquid-air contact on the weft face
f_1^f	Area fraction of liquid-solid contact (filament)
f_2^f	Area fraction of liquid-air contact on filament
f_1^{wp}	Area fraction of liquid-solid contact (warp yarn)
f_1^{wf}	Area fraction of liquid-solid contact (weft yarn)
f_1	Area fraction of liquid-solid contact
f_2	Area fraction of liquid-air contact
f_{11}^{wp}	Area fraction of liquid-solid contact (warp) in yarn configuration I
f_{12}^{wp}	Area fraction of liquid-solid contact (warp) in yarn configuration II
f_{13}^{wp}	Area fraction of liquid-solid contact (warp) in yarn configuration III
f_{11}^{wf}	Area fraction of liquid-solid contact (weft) in yarn configuration I
f_{12}^{wf}	Area fraction of liquid-solid contact (weft) in yarn configuration II
f_{13}^{wf}	Area fraction of liquid-solid contact (weft) in yarn configuration III
f_{21}	Area fraction of liquid-air in yarn configuration I
f_{22}	Area fraction of liquid-air in yarn configuration II
f_{23}	Area fraction of liquid-air in yarn configuration III
F_f	Force applied by the fiber in Wilhelmy's method
g	Acceleration due to gravity
N	Total yarn configuration repeats in a weave unit
n_1	Repeats of yarn configuration I in a weave unit

(*continued on next page*)

(*continued*)

Nomenclature	
n_2	Repeats of yarn configuration II in a weave unit
n_3	Repeats of yarn configuration III in a weave unit
P_{wp}	Inter-yarn distance between warp yarn
P_{wf}	Inter-yarn distance between the weft yarn
r	Radius of filament
r_ψ	Roughness of wetted solid-liquid interface
R	Radius of curvature of the liquid meniscus between filaments
R'	Radius of curvature of the liquid meniscus between yarns
S	Spacing ratio
T_y	Twist per unit length
T_y^{wp}	Twist per unit length in warp yarn
T_y^{wf}	Twist per unit length in the weft yarn
V	Volume of the droplet
V_f	Yarn packing fraction
V_{f_o}	Minimum yarn packing fraction
V_{f_m}	Maximum possible yarn packing fraction of a twisted yarn
wp	Warp yarn
wf	Weft yarn
WP	Warp-rich face of the fabric
WF	Weft-rich face of the fabric

CRediT authorship contribution statement

Siddharth Shukla: Writing – review & editing, Writing – original draft, Visualization, Validation, Software, Methodology, Investigation, Formal analysis, Data curation, Conceptualization. **Yue Wen:** Visualization, Software, Investigation, Data curation. **Imre Szenti:** Visualization, Software, Investigation, Data curation. **Akos Kukovecz:** Writing – review & editing, Supervision, Resources, Funding acquisition. **Thomas C. Sykes:** Writing – review & editing, Supervision, Resources. **Rhodri Jervis:** Writing – review & editing, Writing – original draft, Supervision, Resources, Project administration, Methodology, Investigation, Funding acquisition. **Amit Rawal:** Writing – review & editing, Writing – original draft, Supervision, Resources, Project administration, Methodology, Investigation, Funding acquisition, Formal analysis, Conceptualization.

Declaration of competing interest

The authors declare that they have no known competing financial interests or personal relationships that could have appeared to influence the work reported in this paper.

Acknowledgements

This work was supported by the University College London–IIT Delhi (UCL-IITD) Strategic Partnership MFIRP grant (MI02467G) from the Industrial Research and Development Unit, Indian Institute of Technology Delhi. AK acknowledges project no. RRF-2.3.1-21-2022-00009, titled National Laboratory for Renewable Energy that has been implemented with the financial support provided by the Recovery and Resilience Facility of the European Union within the framework of Programme Széchenyi Plan Plus. RJ and YW acknowledge the Engineering and Physical Sciences Research Council (EPSRC) for funding under grant number EP/W033321/1. Also, thanks to Prof. David Seveno for providing the Kevlar/PTFE hybrid woven sample and granting access to the COMPLEXURF research lab at KU Leuven, Belgium, to conduct single-fiber contact angle measurements.

Appendix A. Supplementary material

Supplementary data to this article can be found online at https://doi.org/10.1016/j.matdes.2025.114519.

Data availability

Data will be made available on request.

References

[1] T. Young III, An essay on the cohesion of fluids, Phil. Trans. R. Soc. 95 (1805) 65–87, https://doi.org/10.1098/rstl.1805.0005.
[2] K.-Y. Law, Definitions for hydrophilicity, hydrophobicity, and superhydrophobicity: getting the basics right, J. Phys. Chem. Lett. 5 (2014) 686–688, https://doi.org/10.1021/jz402762h.
[3] D. Ahmad, I. Van Den Boogaert, J. Miller, R. Presswell, H. Jouhara, Hydrophilic and hydrophobic materials and their applications, Energy Sources Part A 40 (2018) 2686–2725, https://doi.org/10.1080/15567036.2018.1511642.
[4] J. Kijlstra, K. Reihs, A. Klamt, Roughness and topology of ultra-hydrophobic surfaces, Colloids Surf A Physicochem Eng Asp 206 (2002) 521–529.
[5] R.N. Wenzel, Resistance of solid surfaces to wetting by water, Ind. Eng. Chem. 28 (1936) 988–994, https://doi.org/10.1021/ie50320a024.
[6] A.B.D. Cassie, S. Baxter, Wettability of porous surfaces, Trans. Faraday Soc. 40 (1944) 546.
[7] R.E. Johnson, R.H. Dettre, Contact angle hysteresis, I. Study of an idealized rough surface, Adv. Chem. 43 (Ser 1964,) 112.
[8] A. Tuteja, W. Choi, M. Ma, J.M. Mabry, S.A. Mazzella, G.C. Rutledge, G. H. McKinley, R.E. Cohen, Designing Superoleophobic Surfaces, Science 318 (2007) 1618–1622, https://doi.org/10.1126/science.1148326.
[9] S. Herminghaus, Roughness-induced non-wetting, Europhys. Lett. 52 (2000) 165.
[10] J. Bico, U. Thiele, D. Quéré, Wetting of textured surfaces, Colloids Surf A Physicochem Eng Asp 206 (2002) 41–46.
[11] N.A. Patankar, Mimicking the Lotus effect: Influence of double Roughness Structures and Slender Pillars, Langmuir 20 (2004) 8209–8213, https://doi.org/10.1021/la048629t.
[12] A. Rawal, S. Sharma, V. Kumar, H. Saraswat, Designing superhydrophobic disordered arrays of fibers with hierarchical roughness and low-surface-energy, Appl. Surf. Sci. 389 (2016) 469–476.
[13] A. Rawal, S. Shukla, S. Sharma, D. Singh, Y.-M. Lin, J. Hao, G.C. Rutledge, L. Vásárhelyi, G. Kozma, A. Kukovecz, Metastable wetting model of electrospun mats with wrinkled fibers, Appl. Surf. Sci. 551 (2021) 149147.
[14] S. Park, J. Kim, C.H. Park, Influence of micro and nano-scale roughness on hydrophobicity of a plasma-treated woven fabric, Text. Res. J. 87 (2017) 193–207, https://doi.org/10.1177/0040517515627169.
[15] M.H. Shim, J. Kim, C.H. Park, The effects of surface energy and roughness on the hydrophobicity of woven fabrics, Text. Res. J. 84 (2014) 1268–1278, https://doi.org/10.1177/0040517513495945.
[16] A.M. Jonas, R. Cai, R. Vermeyen, B. Nysten, M. Vanneste, D. De Smet, K. Glinel, How roughness controls the water repellency of woven fabrics, Mater. Des. 187 (2020) 108389.
[17] S. Michielsen, H.J. Lee, Design of a superhydrophobic surface using woven structures, Langmuir 23 (2007) 6004–6010, https://doi.org/10.1021/la063157z.
[18] S. Brnada, T. Pušić, T. Dekanić, S. Kovačević, Impact of fabric construction on adsorption and spreading of liquid contaminations, Materials 15 (2022) 1998.
[19] M.M.B. Hasan, A. Calvimontes, A. Synytska, V. Dutschk, Effects of topographic structure on wettability of differently woven fabrics, Text. Res. J. 78 (2008) 996–1003, https://doi.org/10.1177/0040517507087851.
[20] Y. Liu, C.A. Fuentes, A.W. Van Vuure, D. Zhang, D. Seveno, Wettability of a hybrid PTFE/Kevlar fabrics at micro-, meso-, and macroscales, Appl. Surf. Sci. 604 (2022) 154613.
[21] L. Gao, T.J. McCarthy, "Artificial lotus leaf" prepared using a, 1945 patent and a commercial textile, Langmuir 22 (2006) (1945) 5998–6000, https://doi.org/10.1021/la061237x.
[22] Governments endorse global PFOA ban, with some exemptions, C&EN Global Enterp 97 (2019) 5, https://doi.org/10.1021/cen-09719-leadcon.
[23] S. Shabanian, B. Khatir, A. Nisar, K. Golovin, Rational design of perfluorocarbon-free oleophobic textiles, Nat. Sustainability 3 (2020) 1059–1066.
[24] S. Baxter, A.B.D. Cassie, The water repellency of fabrics and a new water repellency test, J. Textile Inst. Trans. 36 (1945) T67–T90, https://doi.org/10.1080/19447024508659707.
[25] J.A. Kleingartner, S. Srinivasan, Q.T. Truong, M. Sieber, R.E. Cohen, G. H. McKinley, Designing robust hierarchically textured oleophobic fabrics, Langmuir 31 (2015) 13201–13213, https://doi.org/10.1021/acs.langmuir.5b03000.
[26] R.N. Darie-Niță, M. Răpă, S. Frąckowiak, Special features of polyester-based materials for medical applications, Polymers 14 (2022) 951.
[27] B. Zhang, Y. Jiang, Durable antibacterial and hydrophobic polyester fibres and wearable textiles, Micro Nano Lett. 13 (2018) 1011–1016, https://doi.org/10.1049/mnl.2018.0197.
[28] E. Gauthier, Q. Duan, T. Hellstern, J. Benziger, Water flow in, through, and around the gas diffusion layer, Fuel Cells 12 (2012) 835–847, https://doi.org/10.1002/fuce.201100187.
[29] K. Hiyoto, S.M. Sorna, A. Maksot, R.G. Reifenberger, C.-S.-J. Tsai, E.R. Fisher, Effects of surface hydrophobicity of lab coat fabrics on nanoparticle attachment and resuspension: implications for fabrics used for making protective Clothing or Work Uniform, ACS Appl. Nano Mater. 6 (2023) 7384–7394, https://doi.org/10.1021/acsanm.3c00470.
[30] S. Schellenberger, P.J. Hill, O. Levenstam, P. Gillgard, I.T. Cousins, M. Taylor, R. S. Blackburn, Highly fluorinated chemicals in functional textiles can be replaced by re-evaluating liquid repellency and end-user requirements, J. Clean. Prod. 217 (2019) 134–143, https://doi.org/10.1016/j.jclepro.2019.01.160.
[31] W.X. Voo, W.C. Chong, H.C. Teoh, W.J. Lau, Y.J. Chan, Y.T. Chung, Facile Preparation of durable and Eco-Friendly Superhydrophobic Filter with Self-Healing

Ability for Efficient Oil/Water Separation, Membranes 13 (2023) 793, https://doi.org/10.3390/membranes13090793.
[32] W.J. Shanahan, J.W.S. Hearle, An energy method for calculations in fabric mechanics part II: examples of application of the method to woven fabrics, J. Text. Inst. 69 (1978) 92–100.
[33] X. Chen, H. Wang, Modelling and computer-aided design of 3D hollow woven reinforcement for composites, J. Text. Inst. 97 (2006) 79–87.
[34] J. Lu, M. Qiu, Y. Li, Wear models and mechanical analysis of PTFE/Kevlar fabric woven liners used in radial spherical plain bearings, Wear 364–365 (2016) 57–72.
[35] D.B. Clark, B. Miller, Liquid transport through fabrics; wetting and steady-state flow: Part II: fabric wetting, Text. Res. J. 48 (1978) 256–260.
[36] N. Pan, Development of a constitutive theory for short fiber yarns: mechanics of staple yarn without slippage effect, Text. Res. J. 62 (1992) 749–765, https://doi.org/10.1177/004051759206201208.
[37] R. Tadmor, Line energy and the relation between advancing, receding, and young contact angles, Langmuir 20 (2004) 7659–7664, https://doi.org/10.1021/la049410h.
[38] W. Watson, Z. Grosicki, Watson's Textile design and colour: elementary weaves and figured fabrics, [Seventh edition], Woodhead Pub, Cambridge, 2004.
[39] W. Watson, Z. Grosicki, Watson's advanced textile design: compound woven structures, [fourth edition], Woodhead Publishing, Abington, 2004.
[40] A. Ferrari, I. Lunati, Inertial effects during irreversible meniscus reconfiguration in angular pores, Adv. Water Resour. 74 (2014) 1–13, https://doi.org/10.1016/j.advwatres.2014.07.009.
[41] W. Choi, A. Tuteja, S. Chhatre, J.M. Mabry, R.E. Cohen, G.H. McKinley, Fabrics with tunable oleophobicity, Adv. Mater. 21 (2009) 2190–2195, https://doi.org/10.1002/adma.200802502.
[42] N. Otsu, A threshold selection method from gray-level histograms, IEEE Trans. Syst. Man Cybern. 9 (1979) 62–66.
[43] L. Wilhelmy, Ueber die abhängigkeit der capillaritäts-constanten des alkohols von substanz und gestalt des benetzten festen körpers, Ann. Phys. 195 (1863) 177–217, https://doi.org/10.1002/andp.18631950602.
[44] B. Miller, R.A. Young, Methodology for studying the wettability of filaments, Text. Res. J. 45 (1975) 359–365, https://doi.org/10.1177/004051757504500501.
[45] C.A. Schneider, W.S. Rasband, K.W. Eliceiri, NIH image to ImageJ: 25 years of image analysis, Nat. Methods 9 (2012) 671–675, https://doi.org/10.1038/nmeth.2089.
[46] S. Sharma, A. Rawal, I.Y. Tóth, L. Vásárhelyi, G. Kozma, Á. Kukovecz, S. Jee, F. Ayaydin, Superhydrophobic self-similar nonwoven-titanate nanostructured materials, J. Colloid Interface Sci. 598 (2021) 93–103.
[47] S.V. Lomov, G. Huysmans, I. Verpoest, Hierarchy of textile structures and architecture of fabric geometric models, Text. Res. J. 71 (2001) 534–543, https://doi.org/10.1177/004051750107100611.
[48] S. Shabanian, X. Zhao, S. Au, N.T. Furtak, K. Golovin, Sustainable design of non-fluorinated yet oleophobic fibrous surfaces, J. Mater. Chem. A 12 (2024) 15716–15730, https://doi.org/10.1039/D4TA01659A.
[49] C.-C. Tsai, Y. Gu, K.G. Kornev, Wetting of nanofiber yarns, Colloids Surf A Physicochem Eng Asp 459 (2014) 22–30, https://doi.org/10.1016/j.colsurfa.2014.06.037.
[50] S. Rebouillat, B. Letellier, B. Steffenino, Wettability of single fibers-beyond the contact angle approach, Int. J. Adhesion Adhesives 19 (1999) 303–314, https://doi.org/10.1016/S0143-7496(99)00006-8.
[51] T. Gilet, D. Terwagne, N. Vandewalle, Droplets sliding on fibres, Eur. Phys. J. E 31 (2010) 253–262, https://doi.org/10.1140/epje/i2010-10563-9.
[52] K. Van De Velde, P. Kiekens, Wettability of natural fibres used as reinforcement for composites, Angew. Makromol. Chem. 272 (1999) 87–93, https://doi.org/10.1002/(SICI)1522-9505(19991201)272:1<87::AID-APMC87>3.0.CO;2-Q.
[53] S. Qiu, C.A. Fuentes, D. Zhang, A.W. Van Vuure, D. Seveno, Wettability of a single carbon fiber, Langmuir 32 (2016) 9697–9705, https://doi.org/10.1021/acs.langmuir.6b02072.
[54] J. Wang, C.A. Fuentes, D. Zhang, X. Wang, A.W. Van Vuure, D. Seveno, Wettability of carbon fibres at micro- and mesoscales, Carbon 120 (2017) 438–446, https://doi.org/10.1016/j.carbon.2017.05.055.
[55] C.A. Fuentes, M. Hatipogullari, S. Van Hoof, Y. Vitry, S. Dehaeck, V. Du Bois, P. Lambert, P. Colinet, D. Seveno, A.W. Van Vuure, Contact line stick-slip motion and meniscus evolution on micrometer-size wavy fibres, J. Colloid Interface Sci. 540 (2019) 544–553, https://doi.org/10.1016/j.jcis.2019.01.045.
[56] H. Tavana, G. Yang, C.M. Yip, D. Appelhans, S. Zschoche, K. Grundke, M.L. Hair, A. W. Neumann, Stick−slip of the three-phase line in measurements of dynamic contact angles, Langmuir 22 (2006) 628–636, https://doi.org/10.1021/la051715o.
[57] M.E.R. Shanahan, Simple theory of "stick-slip" wetting hysteresis, Langmuir 11 (1995) 1041–1043, https://doi.org/10.1021/la00003a057.
[58] B.B. Sauer, T.E. Carney, Dynamic contact angle measurements on glass fibers: influence of fiber diameter on hysteresis and contact line pinning, Langmuir 6 (1990) 1002–1007, https://doi.org/10.1021/la00095a020.
[59] Q. Wei, Y. Liu, D. Hou, F. Huang, Dynamic wetting behavior of plasma treated PET fibers, J. Mater. Process. Technol. 194 (2007) 89–92, https://doi.org/10.1016/j.jmatprotec.2007.04.001.
[60] B. Bhushan, M. Nosonovsky, The rose petal effect and the modes of superhydrophobicity, Phil. Trans. R. Soc. A 368 (2010) 4713–4728, https://doi.org/10.1098/rsta.2010.0203.
[61] Y.-L. Hsieh, M. Wu, D. Andres, Wetting characteristics of poly(p-phenylene terephthalamide) single fibers and their adhesion to epoxy, J. Colloid Interface Sci. 144 (1991) 127–144, https://doi.org/10.1016/0021-9797(91)90243-2.
[62] S. Lomov, D. Ivanov, I. Verpoest, M. Zako, T. Kurashiki, H. Nakai, S. Hirosawa, Meso-FE modelling of textile composites: road map, data flow and algorithms, Compos. Sci. Technol. 67 (2007) 1870–1891, https://doi.org/10.1016/j.compscitech.2006.10.017.
[63] S. Chwastiak, A wicking method for measuring wetting properties of carbon yarns, J. Colloid Interface Sci. 42 (1973) 298–309, https://doi.org/10.1016/0021-9797(73)90293-2.
[64] V. Neacsu, A. Abu Obaid, S.G. Advani, Spontaneous radial capillary impregnation across a bank of aligned micro-cylinders – Part I: theory and model development, Int. J. Multiph. Flow 32 (2006) 661–676, https://doi.org/10.1016/j.ijmultiphaseflow.2006.02.006.
[65] M.R. Piggott, Short fibre polymer composites: a fracture-based theory of fibre reinforcement, J. Compos. Mater. 28 (1994) 588–606.
[66] H.M. Princen, Capillary phenomena in assemblies of parallel cylinders: III. liquid columns between horizontal parallel cylinders, J. Colloid Interface Sci. 34 (1970) 171–184, https://doi.org/10.1016/0021-9797(70)90167-0.
[67] C. Duprat, S. Protière, A.Y. Beebe, H.A. Stone, Wetting of flexible fibre arrays, Nature 482 (2012) 510–513, https://doi.org/10.1038/nature10779.
[68] B. Bhushan, E.K. Her, Fabrication of superhydrophobic surfaces with high and low adhesion inspired from rose petal, Langmuir 26 (2010) 8207–8217, https://doi.org/10.1021/la904585j.
[69] L. Feng, Y. Zhang, J. Xi, Y. Zhu, N. Wang, F. Xia, L. Jiang, Petal effect: a superhydrophobic state with high adhesive force, Langmuir 24 (2008) 4114–4119, https://doi.org/10.1021/la703821h.
[70] A. Lafuma, D. Quéré, Superhydrophobic states, Nature Mater 2 (2003) 457–460, https://doi.org/10.1038/nmat924.
[71] T.C. Sykes, B.D. Fudge, M.A. Quetzeri-Santiago, J.R. Castrejón-Pita, A.A. Castrejón-Pita, Droplet splashing on curved substrates, J. Colloid Interface Sci. 615 (2022) 227–235, https://doi.org/10.1016/j.jcis.2022.01.136.
[72] C.G.L. Furmidge, Studies at phase interfaces. I. the sliding of liquid drops on solid surfaces and a theory for spray retention, J. Colloid Sci. 17 (1962) 309–324, https://doi.org/10.1016/0095-8522(62)90011-9.
[73] K. Kawasaki, Study of wettability of polymers by sliding of water drop, J. Colloid Sci. 15 (1960) 402–407, https://doi.org/10.1016/0095-8522(60)90044-1.
[74] C.W. Extrand, A.N. Gent, Retention of liquid drops by solid surfaces, J. Colloid Interface Sci. 138 (1990) 431–442, https://doi.org/10.1016/0021-9797(90)90225-D.
[75] W. Choi, A. Tuteja, J.M. Mabry, R.E. Cohen, G.H. McKinley, A modified Cassie–Baxter relationship to explain contact angle hysteresis and anisotropy on non-wetting textured surfaces, J. Colloid Interface Sci. 339 (2009) 208–216, https://doi.org/10.1016/j.jcis.2009.07.027.